Electric Vehicle Power Trains:

High-Performance Control for Constant Power Load Stabilization

by

Matias Anun

Ing., Universidad Nacional de Córdoba, 2010

A THESIS SUBMITTED IN PARTIAL FULFILLMENT OF
THE REQUIREMENTS FOR THE DEGREE OF

MASTER OF APPLIED SCIENCE

in

The Faculty of Graduate and Postdoctoral Studies

(Electrical & Computer Engineering)

THE UNIVERSITY OF BRITISH COLUMBIA

(Vancouver)

August 2014

Abstract

The development of sustainable transport systems has experienced great improvements in the last 15 years. As a result, electric vehicles, namely hybrid electric vehicles (HEVs) and all-electric or battery electric vehicles (BEVs), are slowly starting to coexist with regular internal combustion vehicles around the world. The complex powering structure of automotive electric systems can be described as a distributed multi-converter architecture. In pursuit of performance, constant-power behavior of tightly regulated downstream converters has raised as an important challenge in terms of system stability and controllability.

The first part of this work presents the theory and experimental validation of the unstable behavior introduced by constant-power loads (CPLs) in power converters, more precisely in a Buck+Boost cascade converter as the battery charge/discharge unit. Open-loop instability with CPLs is studied in asynchronous and synchronous operating modes identifying this latter as a highly destructive scenario that creates undesirable unbounded oscillatory behavior.

The second part of this work presents the derivation of the Circular Switching Surfaces (CSS) and the implementation of the CSS-based control technique for CPL stabilization. The analysis shows that the constant-power load trajectories and the proposed CSS present a wide, stable operating area and near-optimal transient response. Furthermore, impedance analysis of the converter in close-loop control shows advantageous reduced output source impedance. This extremely high dynamic capability prevents the use of bulky DC capacitors for bus stabilization, and allows the implementation of metal-film capacitors, which have reliability advantages over commonly employed electrolytic capacitors, as well as reduced ESR to improve system efficiency. Beyond the improved stabilization properties of the

proposed CCS-based controller, a comparison with traditional compensated linear controller and non-linear SMC highlights significant improvements in terms of dynamic response for sudden CPL changes. The analysis in this thesis is done in a normalized converter to provide generality to the results and is valid for any power rating. Simulation and experimental results are provided to validate the work.

The last part of this thesis work presents the design, construction, and testing of a high-power 3-phase converter. This platform is intended for electric motor driving and is able to manage $20kW$ of power flow and above, making it suitable for high power traction system development. The platform features an Intelligent Power Module (IPM) to provide with flexibility allowing for changing the power module according to the requirements of the development. Testing of the platform was done in a $0.5HP$ AC induction motor drive controlled with Voltz-per-Hertz control technique. The integration of the BCDU and the high-power 3-phase motor drive platform conform a high-power bidirectional motor drive platform for the development and testing of control techniques for energy management in EV.

Preface

This work is based on research performed at the Electrical and Computer Engineering Department of the University of British Columbia by Matias Anun, under the supervision of Dr. Martin Ordonez. Some experimental validation work was done in collaboration with Ignacio Galiano Zurbriggen.

A version of Chapters 1 and 2 has been published at the IEEE Applied Power Electronics Conference and Exposition (APEC) 2014 [1], and was submitted to a power electronics journal [2].

Chapter 3 is based on the collaboration project between Future Vehicles Technologies Co. and Matias Anun under the supervision of Dr. Martin Ordonez and the technical collaboration of Peter Ksiazek. Hardware design, assembly and testing of the power platform was done by Matias Anun.

As first author of the above-mentioned publications and work, the author of this thesis developed the theoretical concepts and wrote the manuscripts, receiving advice and technical guidance from Dr. Martin Ordonez. The author developed simulations and experimental platforms, receiving contributions from Dr. Ordonez's research team, in particular from the PhD. student Ignacio Galiano Zurbriggen, who assisted the author in the development of some experimental tasks.

Table of Contents

List of Tables

List of Figures

Acknowledgments

I would like to thank my supervisor Dr. Martin Ordonez for recruiting me as part of his research team. His support, extreme patience, and drive were a fundamental guiding light during the development of my Master's program.

I would also like to acknowledge my lab mates from the Alpha Technology Power Laboratory for sharing their experience and knowledge, making these years a fulfilling period. In particular, thanks go to my old friend Ignacio Galiano Zurbriggen. Without his input and backup, this outcome would not have been possible.

I want to express my deepest gratitude to my parents Monica and Simon and to my brother Joaquin for their unconditional love and understanding. I could not have made it through this learning experience without their continuous support. To my girlfriend Vanesa, thank-you for enduring a long-distance relationship for these couple of years.

For my parents

Chapter 1

Introduction

1.1 Motivation

Increasing concern for the environment, as well as rise in the fossil-fuel prices have pushed societies to seek alternative means of transportation to reduce oil dependence and diminish air pollution. As a result, the development of a sustainable transport system has experienced great improvements in the last 15 years. Electric vehicles (EVs), namely hybrid electric vehicles (HEVs) and all-electric or battery-electric vehicles (BEVs), are slowly starting to coexist with regular internal combustion vehicles around the world [3–5].

EVs present several alternatives for the implementation of the propulsion system. Besides using more than one energy source for propulsion, HEVs combine and Internal Combustion Engine (ICE) with an electric motor in a parallel or series architecture to improve fuel efficiency and lower emissions compared to regular ICE vehicles. In BEVs, the traction system relies solely on electric motors, eliminating any emission generation. For this reason, BEVs are usually called zero-emission vehicles (ZEVs). A purely EV presents the following characteristics:

No exhaust pollutant emissions.

High level of efficiency.

Reduced maintenance for battery and electric motor systems.

Virtually zero maintenance required for the associated electronics.

No oil changes and cleaner operation.

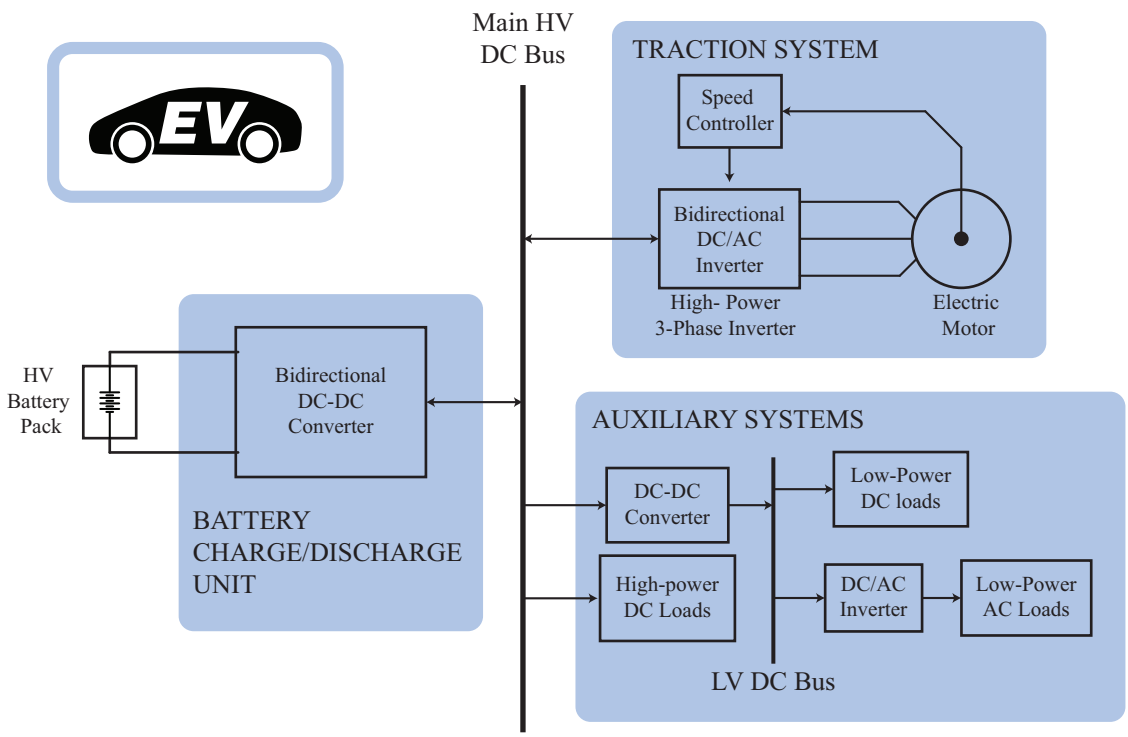

Figure 1.1: Simplfied block diagram of the power structure of a BEV.

Longer brake lifetime with regenerative and dynamic braking.

Minimized noise pollution.

BEVs have reported efficiency levels as high as 90% while conventional vehicles (CVs) is 35% at best, making the former the ultimate solution to create a green and sustainable transport system. The reason for the fast growth of HEVs is their profitability for the industry and affordability for consumers, allowing their introduction to the automotive market. HEVs can be thought of as an intermediate stage between CVs and BEVs (purely EVs).

Driven by advances in power electronics, which have allowed the development of power converters with high levels of efficiency and reliability, the power structure of electric vehicles has clearly evolved to a power electronics's intensive solution, relying almost exclusively on the electric implementation for automotive subsystems. In advanced automotive structures, besides the electric propulsion system, several electrical subsystems are used for control, safety and comfort in the vehicle. The relatively complex power structure of automotive

electric systems can be described as a distributed multi-converter scheme including DC as well as AC subsystems [6, 7]. A simplified block diagram of the distributed system of a BEV is illustrated in Fig. 1.1, where the main DC bus feeds the electric motor drive and downstream converters, which power different automotive electric subsystems.

To provide energy from the source to the electric system, a smart and efficient interface is required to achieve reliable and high-quality power flow. Depending on the characteristics of the energy source and the requirements of the DC link, a particular DC-DC converter is required to perform the voltage conversion ratio. Moreover, in advanced systems the interface, denominated Battery Charge/Discharge Unit (BCDU), provides the means for recovering energy from the traction system to the energy storage (regenerative braking) through bidirectionality in the converter, highly improving energy usage.

1.2 Literature Review

As an emerging trend currently in development, different technologies and approaches can be found for the design, implementation and control of BEVs, all achieving particular advantages and breakthroughs in performance.

As was shown before, the power structure of EV systems has become complex in its implementation and it will continue to expand to include new features. The high complexity of the system combined with the latest advances in power electronics have created important challenges in terms of system design and controllability, where high-performance controllers are required not only to increase efficiency and competitiveness, but to provide reliable operation with dynamic stability.

The following literature review identifies the state-of-the-art technology for power flow management in EV systems, focusing on the electric power train and battery interface. In addition, it presents a complete review on the research done on the existence and behavior of constant-power loads (CPLs), and on the current techniques developed for CPL stabilization

Vehicle	Battery type	Energy [kWh]	Nominal Voltage [V]
Smart	Li-ion	17.6	370
Nissan Leaf	Li-ion	24	360
Testla Model S	Li-ion	85	375
Ford Focus	Li-ion	23	325
Toyota Prius	Ni-MH	4.4	201.6
Honda Insight	Ni-MH	0.58	100.8
BMW i3	Li-ion	22	380

Table 1.1: EVs energy storage system characteristics

in automotive systems.

1.2.1 Battery Charge/Discharge Units

EVs are propelled using bidirectional DC-DC converters as BCDU to interface energy storage systems, such as batteries, with the main DC bus [8]. These converters are suitable for controlling power flow in motoring and regenerative braking operation to improve the overall system efficiency and travel range. Two battery technologies predominate in the EV market and are shown in Table 1.1. However, Ni-MH most likely be displaced by Li-Ion in the upcoming generation of EVs as, besides presenting higher energy and power density and reducing total weight (critical parameter for EV application) than Ni-MH, Li-Ion has become more reliable [9].

The nominal DC-link voltage is in the range of $400V$ to adapt to the power requirements of the propulsion system [10], and is typically higher than the energy storage voltage, thus step-up operation is required to obtain the DC-link voltage level [11]. However, in cases where the nominal battery output voltage–which depends mainly on the number of cells stacked and presents an approximate variation of $(+15\%, -30\%)$–overlaps with the DC-link voltage required, step-down operation is necessary as well [12]. The Buck+Boost cascade converter depicted in the lower part of Fig. 1.2 is capable of performing step-down and step-up operations and presents enhanced properties such as increased performance and efficiency in comparison to other bidirectional DC-DC converters [13–16].

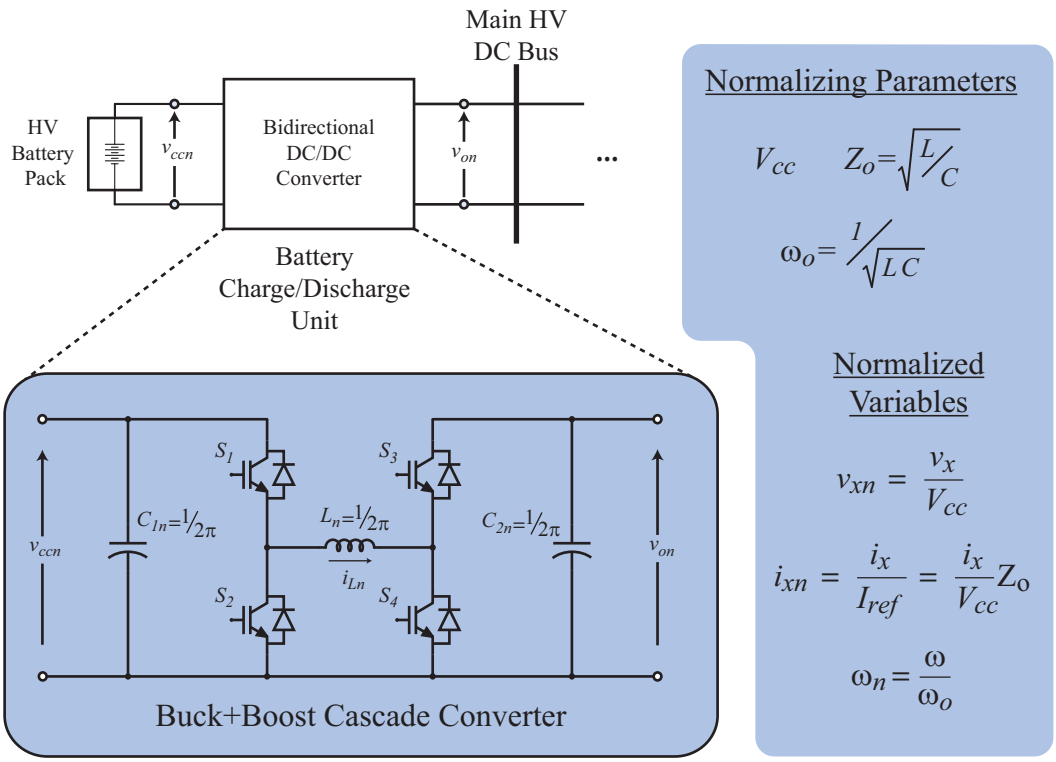

Figure 1.2: Implementation of the BCDU.

Vehicle	Type	Motor type	Power [kW]
Honda Insight	HEV (parallel hybrid)	BLDC	10
Toyota Prius	HEV (series-parallel hybrid)	BLDC	60
Smart Fortwo	BEV	BLDC	55
Nissan Leaf	BEV	BLDC	80
Ford Focus	BEV	BLDC	107
BMW i3	BEV	AC induction	130
Testla Model S	BEV	AC induction	310

Table 1.2: Electric motor implementation and main parameters

1.2.2 CPL in EV Systems

The idea behind more-electric vehicles (MEVs) is to evolve from mechanic and/or hydraulic subsystems to replace them with an electric implementation in order to improve system efficiency and reliability. As a consequence, electric auxiliary systems in EVs have expanded from basic lighting and heating systems to more complex ones including electric steering, dynamic and regenerative braking, active suspension for ride-height control, to mention a few. For these subsystems, power electronics perform ON/OFF switching as well as transforming power form and level. Overall power requirements for EVs auxiliary systems is estimated to increase to more than $3kW$ in the next few years [12].

The traction system in BEVs, on the other hand, consists of a high-power 3-phase DC/AC inverter that draws DC power from the batteries and delivers AC power to the the electric motor, which converter the electrical energy into mechanical energy. For vehicle controllability, a speed/torque control strategy is implemented and controlled with the throttle pedal. Table 1.2 specifies the type of electric machine employed in the most popular EVs in the market of the last 2 years. Power rating is also specified for the traction system, identifying the level of power required by the DC/AC inverter from the batteries. For purely electric EVs, power rating generally exceeds the $50kW$. An HEV motor might require reduced power, depending on the topology of the propulsion system.

As depicted in Fig. 1.1, the BCDU delivers power to the traction system and the auxiliary systems. High-efficiency high-bandwidth power converters fed by the main bus create unique

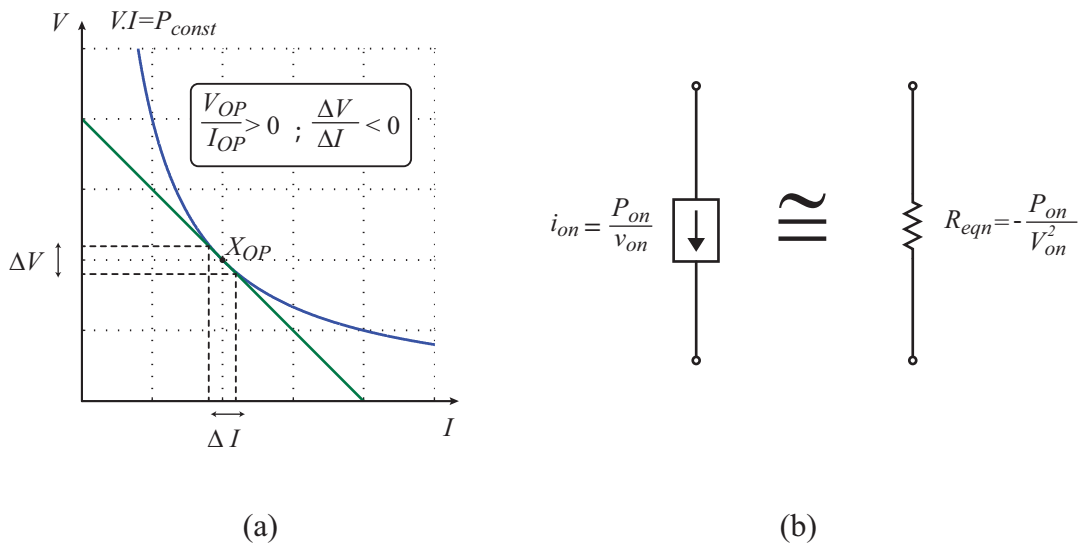

Figure 1.3: Linearization of the CPL characteristic curve (a) allows to model the load as a negative incremental resistor (b) identifying the unstable nature of the load.

upstream dynamic characteristics which have been the subject of study over the past few years. Under tight-speed regulation with constant torque-load relationship, the motor drive exhibits constant power (CP) behavior at the input of the DC bus [17, 18]. A similar situation occurs in downstream converters under tight regulation [19–23]. As shown in Fig. 1.3, the dynamic behavior of CPLs is equivalent to a dynamic negative resistance which, under certain conditions, can produce instability in the DC bus and consequently, in the system [19]. As it is deduced with the linearized model of the CPL, the instability effect is directly proportional to the CP level, hence major concern is focused on the traction system CP behavior in relation to the power levels required for the vehicle's motion. On the other hand, according to the assessment of the limitations of practical CPLs in real world application which have been studied in [20], practical bandwidth limitations play a fundamental role in CP behavior. In this work, an ideal (infinite bandwidth) CPL model is employed in the analysis to account for the worst-case scenario.

1.2.3 CPL Stabilization Methods

Passive stabilization methods have been developed to stabilize the open-loop converter. RC and RL networks were introduced at the resonance frequency of the filter in the converter, increasing the overall damping of the system [20, 21]. Although the method is simple, the addition of elements to the filter reduces efficiency and negatively impacts size and cost. Active stabilization methods were presented in [22–24], which avoid the introduction of additional components. Nevertheless, while these techniques stabilize the open-loop system, a feedback controller is still required to achieve system regulation.

Beyond traditional linear controllers, which rely on a linearization process that limits the validity of the controllers to a small area around the operating point, the analysis developed in [25–27] demonstrates the potential of non-linear techniques to address CPL instability. Boundary controllers have been widely studied and have proven to be robust with large-signal validity [28]. Furthermore, with the correct switching surface selection, remarkable improvements can be made in terms of efficiency and dynamic response [29, 30].

1.3 Contribution of the Work

CPL behavior of tightly-regulated converters is a common scenario in high-performance automotive developments and is still a major concern for the design and implementation of stable and reliable power systems. An additional challenge is optimizing the packing of the complex electromechanical system with the associated power electronics.

The simplest approach consists of adjusting the converter filtering parameters to achieve a stable operating converter, but this penalizes size and cost. Although many techniques have been developed in the past few years to stabilize CP-loaded converters, there is still no unique solution that ensures safe operation under all operating conditions.

This work proposes a simple and practical non-linear control, implementing Circular Switching Surfaces (CSS) to address CPL instability in cascaded DC-DC converters used

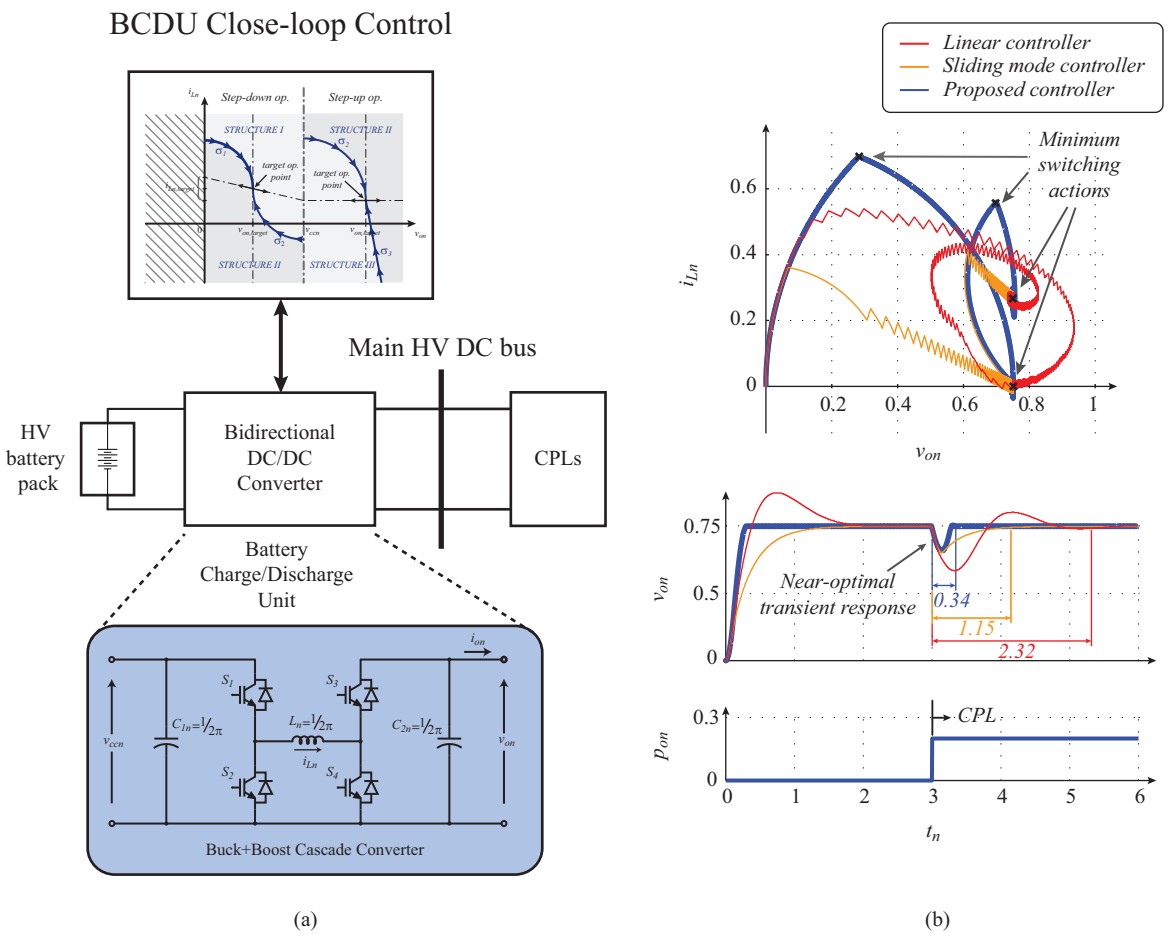

Figure 1.4: The CSS-based closed-loop control implemented in a Buck+Boost cascade converter as BCDU not only to provides high stabilization capabilities for CPL operation, but also remarkably improves performance during transients with respect to recently-proposed linear and non-linear controls.

in electric vehicle power systems as depicted in Fig. 1.4(a). The analysis of switching surfaces goes beyond typical applications with resistive loading studied in [30, 31], as well as undamped systems with constant-current loading studied in [32–34]. Moreover, as shown in Fig. 1.4(b), the control technique proposed provides a solution to constant power loading conditions while achieving outstanding dynamic response in comparison to recently proposed control strategies.

Bulky DC-link capacitance employed to provide system stability can be reduced given the improved large-signal stability achieved by the switching surfaces proposed in this work, highly reducing size and, ultimately, the cost. Furthermore, the proposed switching sur-

faces would allow electrolytic-type capacitors to be replaced by metal-film type capacitors, increasing the reliability of the system [35–39].

It is important to note that the work is developed in a normalized domain depicted in Fig. 1.2, which allows for the extrapolation of the results obtained to any converter, regardless of voltage and current ratings and filter parameters, and ensuring high-performance operation.

Successful development of automotive-oriented power systems requires extensive design and testing stages in order to accomplish reliable and high-performance operation. For this reason, a test bench is fundamental to emulate different working conditions and to validate complete system stability and performance. Through this thesis work, a scaled high-power BCDU and a flexible motor-drive platform were developed to conform an EV power platform. These were used for the experimental validation of the present work.

1.4 Organization

This thesis is organized as follows:

Chapter 2 develops the concept of CPL and the instability effect introduced in power converters. As was determined through the literature review, analysis and experimental results are carried out in a Buck+Boost cascade converter as the BCDU, topology that allows for consideration of any possible configuration regarding energy storage characteristics and DC link requirements. Instability scenarios are analyzed with a linearized Buck+Boost converter loaded with CPL. A more detailed and accurate stability criteria is derived by accounting for inductor resistive losses as well as capacitor ESR, which is normally neglected. Proof of concept is attained with experimental results on a $1kW$ Buck+Boost cascade converter loaded with a fast current load externally controlled to behave as a CPL. Open-loop instability with CPL was studied in asynchronous and synchronous operating modes, identifying the latter as the worst operating condition.

In Chapter 3, the CSS are initially derived and later employed to define the CSS-based

closed-loop control strategy. Stabilization characteristics are analyzed with clarity in the state plane, addressing the operational characteristics for start-up and sudden CPL changes. Time domain simulations are also included. Previous work proposed for CPL stabilization are compared with the proposed technique to establish a benchmark and asses the performance improvements obtained. For the validation of the control technique proposed, several test results are presented. All results were obtained on a $1kW$ Buck+Boost cascade converter.

Chapter 4 presents the design, building and testing of a flexible high-power motor drive platform for EV applications. The platform operates with an Intelligent Power Module (IPM) from Powerex to manage power flow. The board designed to interface the power module integrates voltage, current and temperature measurements, and allows connection with several IPM modules giving the flexibility to adapt the power module according to the requirements. Testing of the platform was done in a $0.5HP$ AC induction motor drive controlled with Voltz-per-Hertz control technique.

Lastly, Chapter 5 presents a summary, remarking on the major outcomes of the work completed within the thesis and outlining future ideas for work.

Chapter 2

Constant-Power Load Instability in BCDU: Theory and Validation

2.1 BCDU Implementation

The Buck+Boost cascade converter, shown in Fig. 2.1, is a bidirectional topology obtained by cascading a Buck with a Boost converter, allowing independent step-down or step-up operation. The different structures of the converter are depicted in Fig. 2.2. In discharge operation (power flow from energy storage to the main DC bus), step-down conversion is obtained by switching between structures I and II. For a step-up operation, structures II and III are employed. The behavior for the converter with CPL is described through the following set of differential equations:

$$\begin{aligned} L\frac{di_L}{dt} &= u_1\ v_{cc} - u_2\ v_o \\ C\frac{dv_o}{dt} &= u_2\ i_L - i_o \end{aligned} \tag{2.1}$$

In (2.1), u represents the state of the switches: $u_1 = 1$ for switches S_1 and S_2, ON and OFF, respectively, and $u_2 = 1$ for switches S_3 and S_4, OFF and ON, respectively.

2.2 Normalized Buck+Boost Cascade Converter

In order to give generality to the development, the converter is normalized, eliminating dependence on converter voltages, currents and power ratings, as well as filter characteristics:

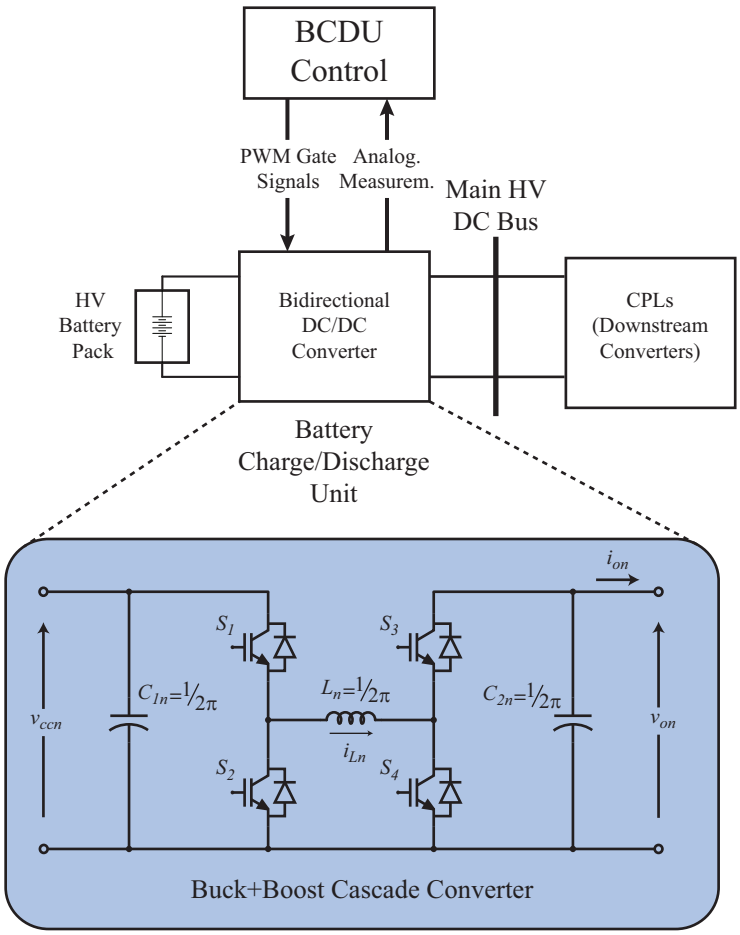

Figure 2.1: BCDU implementation with the Buck+Boost cascade converter presents enhanced properties such as increased performance and efficiency in comparison to other bidirectional DC-DC converters.

$$v_{xn} = \frac{v_x}{V_{cc}} \;\; ; \;\; i_{xn} = \frac{i_x}{I_{ref}} = \frac{i_x}{V_{cc}} Z_o \;\; ; \;\; \omega_n = \frac{\omega}{\omega_0}$$

The normalization procedure makes use of the following base parameters: the input voltage v_{cc}, characteristic impedance of the combined L and C values $Z_o = \sqrt{L/C}$, and the natural resonance period $\omega_0 = {}^1/\sqrt{LC}$. The subindex n is used to indicate normalized variables. Normalizing (2.1) yields the following:

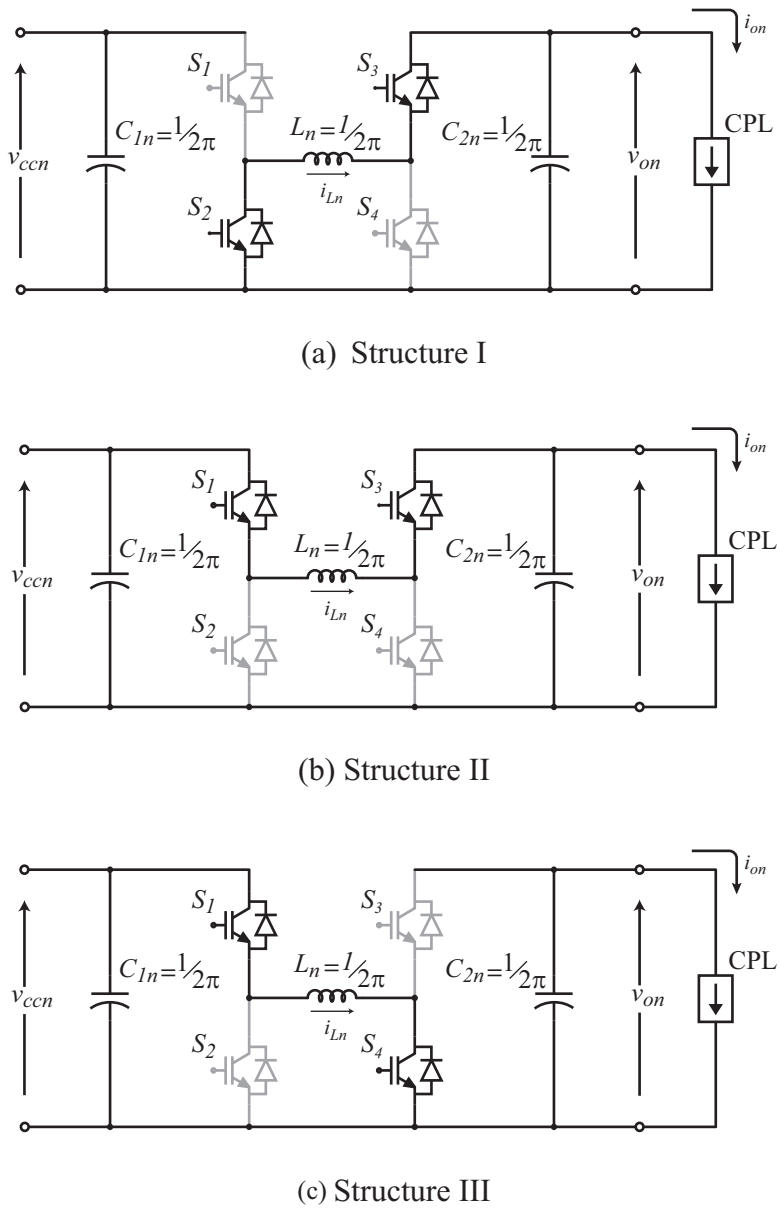

Figure 2.2: Normalized Buck+Boost cascade converter structures (a) $S_2 = S_3 = ON$, (b) $S_1 = S_3 = ON$ and (c) $S_1 = S_4 = ON$.

$$\begin{aligned} \frac{1}{2\pi}\frac{di_{Ln}}{dt_n} &= u_1\ v_{ccn} - u_2\ v_{on} \\ \frac{1}{2\pi}\frac{dv_{on}}{dt_n} &= u_2\ i_{Ln} - i_{on} \end{aligned} \tag{2.2}$$

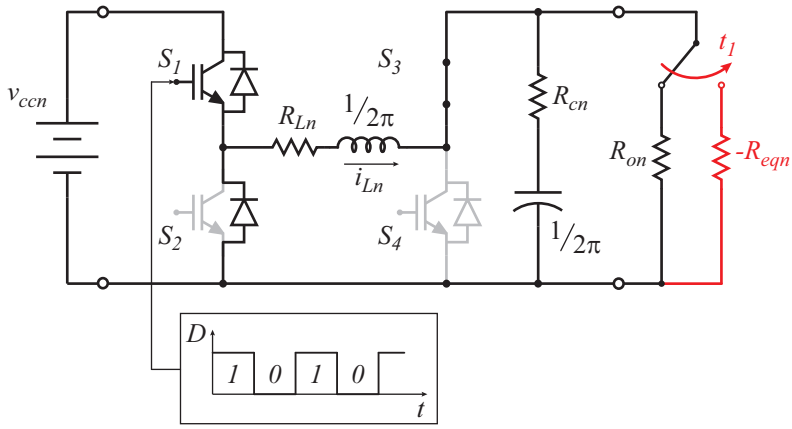

Figure 2.3: The normalized Buck+Boost cascade converter loaded with the linear model of the CPL. Input-to-output transfer function analysis identifies potential right-half-plane poles, depending on the filter parameters.

2.3 CPL Linear Analysis and Open-loop Instability

The presence of CPLs in power converters introduces unique dynamics into the system that are not present with typical resistive or constant current loads, and which generate open-loop instability in the converter. An ideal CPL can be modeled as (2.3) where, for a given operating point (V_{on}, I_{on}), the product of the load voltage and current is kept constant $(P_{on,const} = V_{on}I_{on})$ and the instantaneous value of the load impedance is positive $(R_{on} = {}^{V_{on}}/_{I_{on}})$. A linear approximation is obtained by deriving (2.3) in the small area around (V_{on}, I_{on}), yielding the linear equivalent incremental impedance R_{eqn}. As shown in (2.4), R_{eqn} at the given operating point, or at any other, is negative. The linearized CPL model is (2.5).

$$i_{on} = \frac{P_{on}}{v_{on}} \qquad (2.3) \qquad\qquad \frac{di_{on}}{dv_{on}} = -\frac{P_{on}}{v_{on}^2} = -\frac{1}{R_{eqn}} \qquad (2.4)$$

$$i_{on,lin} = 2\frac{P_{on}}{V_{on}} - \frac{P_{on}}{V_{on}^2}v_{on} = 2I_{on} - \frac{1}{R_{eqn}}v_{on} \qquad (2.5)$$

A cascade converter in step-down operation mode is illustrated in Fig. 2.3(a) with nor-

malized inductor and capacitor parasitic resistances included in the model. By considering the converter loaded with a CPL, and by using the linearized model (2.5), small-signal analysis for the input-to-output transfer function yields the following denormalized result:

$$\frac{\hat{v}_o(s)}{\hat{v}_{cc}(s)} = \frac{R_{eq}}{R_{eq} - R_c} \frac{1}{s^2 LC + s\left[\frac{L}{R_c - R_{eq}} + C\left(R_L + \frac{R_{eq}\, R_c}{R_{eq} - R_c}\right)\right] + \frac{R_L - R_{eq}}{R_c - R_{eq}}} \tag{2.6}$$

Analyzing the roots of the characteristic equation in (2.6), it can be seen that the negative equivalent impedance of the CPL produces a shift in the system's poles which may be displaced to the right-half plane, depending on the filter parameters, making the system open-loop unstable. For a high-efficiency converter, the losses R_L and R_c should remain minimal. Thus, stability of the converter relies on oversizing the output capacitance to comply with the following:

$$\frac{L}{\mid R_c - R_{eq} \mid} < C\left(R_L + \frac{R_{eq}\, R_c}{R_{eq} - R_c}\right) \tag{2.7}$$

Previous criteria is overly conservative and, as a sufficient condition, it ensures stable operation of the open-loop converter.

2.4 Experimental Results

A scaled $1kW$ Buck+Boost cascade converter was implemented in hardware with the parameters indicated in Table I. A fast dynamic CPL with a bandwidth of approximately $25kHz$ was implemented as part of the test bench. A picture of the experimental setup is shown in Fig. 2.4. For a nominal output power of $P_o = 1kW$ and for the filter parameters indicated, the linear stability analysis (2.7) for traditional controllers indicates that the system is highly unstable.

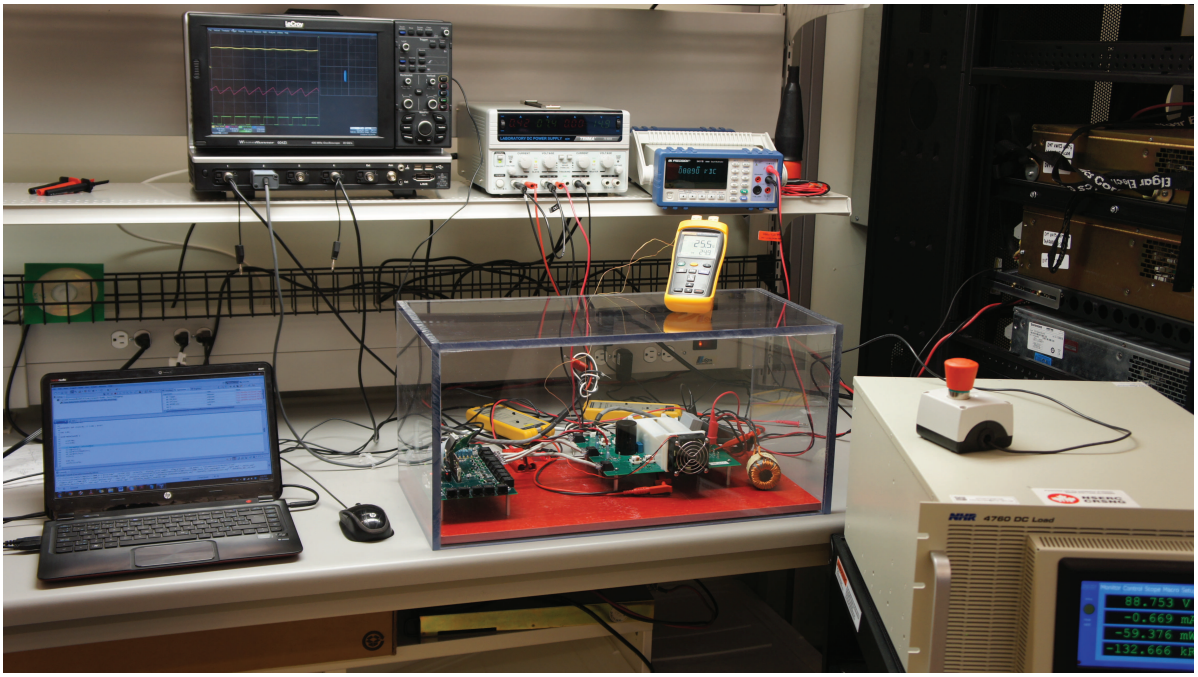

Figure 2.4: Cascade converter experimental setup.

PARAMETER	VALUE
L	$920\mu F$
R_{L-ESR}	0.29Ω
C	$20\mu F$
$R_C(ESR)$	$9m\Omega$
v_o	$90V$
v_{cc}	$50V - 200V$
$P_{o(max)}$	$1kW$

Table 2.1: Platform parameters

Fig. 2.5(b) and 2.6(b) show the experimental results of the cascade converter operating in open loop in asynchronous and synchronous mode, respectively. Switching frequency is set to a fixed value of $f_{sw} = 20kHz$ and duty cycle $D = 0.75$. Operation starts with resistive load R_{on}, and at $t = 3.2ms$, the load switches to CP. As expected, the negative incremental impedance has a negative impact on the stability of the system, producing oscillations at the resonance frequency at the output of the converter. With asynchronous operation (Fig. 2.5(a)), the load dynamics produce an increase in the energy stored by the reactive elements cycle after cycle, increasing the oscillations until the converter enters discontinuous conduction mode (DCM). At this point, the inductor current cannot invert the direction, and remains discharged while the capacitor continues to discharge. This process limits the energy stored in the reactive elements, and the operation quasi-stabilizes after $t \approx 19.2ms$ in a limit cycling which can be observed in the geometric domain.

On the other hand, when switched to synchronous operation (Fig. 2.6(a)), inductor current is allowed to reverse direction. The same loading process is applied, and in this case, the energy in the reactive elements rises without boundaries, increasing the oscillations until the system is shut down using a protection at $t \approx 21ms$. This unbounded and destructive behavior is a major concern that will be addressed by the proposed switching surfaces in the following chapter.

Besides the criteria for stable operation derived previously, the combination of CP as well as regular resistive loads in the power system mitigates CP instability. However, the overall system stability should not rely on the existence of such resistive loads. Practical CPL models differ from (2.4) mainly due to bandwidth limitations of real converters/inverters acting as loads. In current applications (2014), the bandwidth of the CPLs can range from a few Hz to up to few kHz (power supplies connected to the DC Link). This work adopts the worst-case operating scenario of very large CPL bandwidth. If stability and high performance is achieved for the theoretical high bandwidth CPL, then in real world applications, safe operation and rapid response is guaranteed.

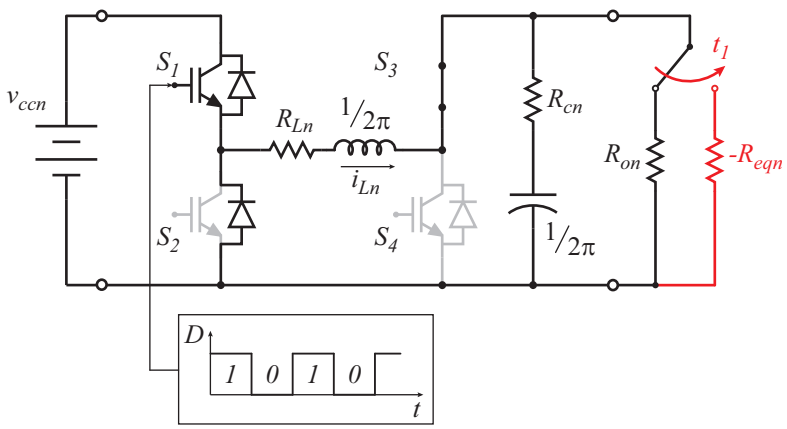

(a)

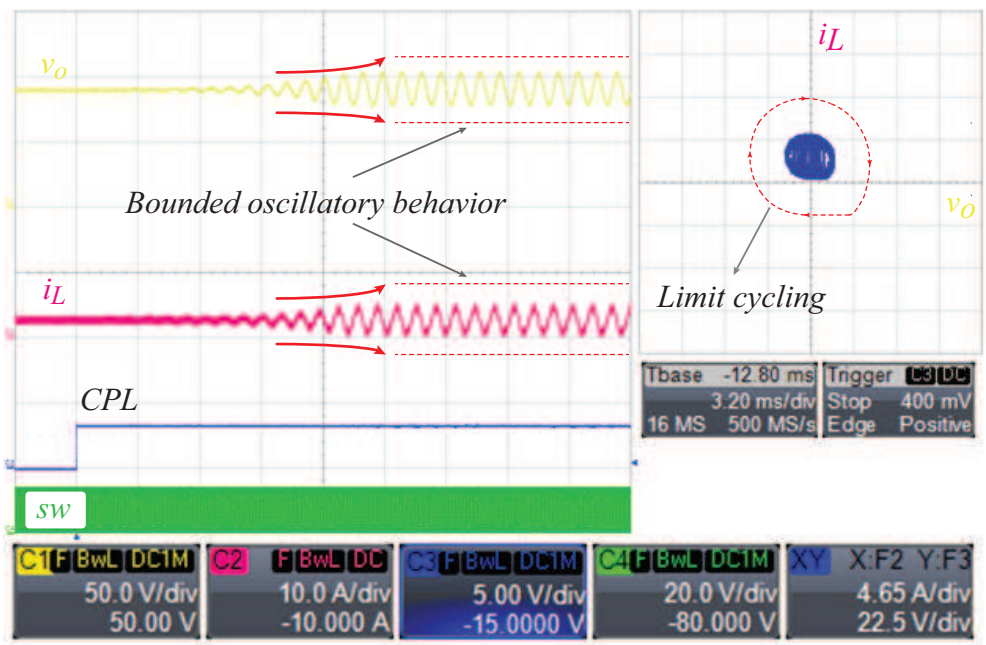

(b)

Figure 2.5: Bounded oscillatory response is obtained for the open-loop cascade converter in asynchronous step-down operation when load is switched from CR to CP.

2.5 Summary

This chapter presented the theory and validation of the unstable behavior introduced by CPL in power converters. The concept was analyzed in a Buck+Boost cascade converter as a BCDU that enables step-up and step-down operation, covering a wide range of possible

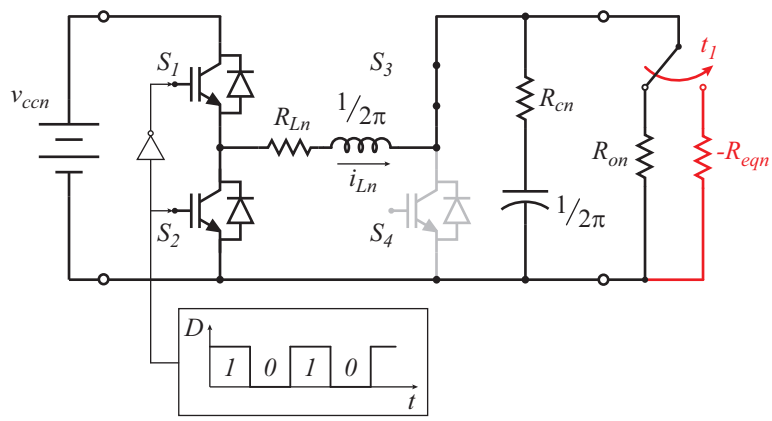

(a)

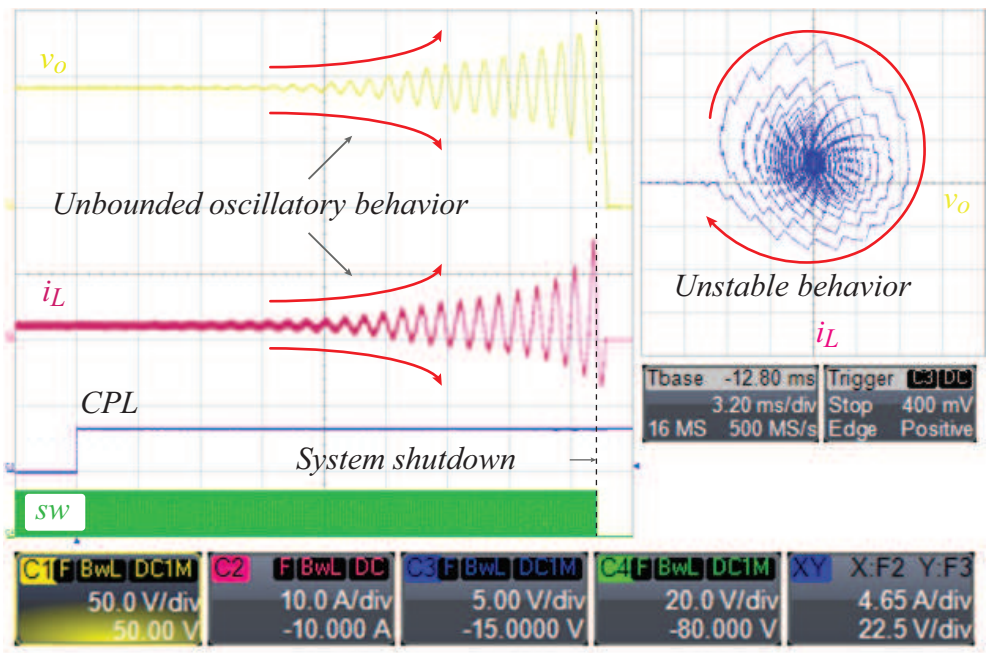

(b)

Figure 2.6: Unbounded oscillatory response is obtained for the open-loop cascade converter in synchronous step-down operation when load is switched from CR to CP.

scenarios, depending on the energy source voltage level and the requirements of the DC link. A normalizing procedure was applied to the converter which was used to generalize the outcomes of the work. To determine instability behavior of the converter loaded with CPL, the load was subject to a linearization process, allowing for computation of the input-to-

output transfer function. Filter parasitic resistances were included in the model, since they play a vital role in system efficiency as well as system stability. With pole-locus analysis a general criteria was obtained to determine the behavior of the converter in open-loop.

The experimental platform was designed with reduced output capacitance, allowing for the use of metal-film caps highly recommended for system reliability. Using the criteria derived for stability, the converter loaded with a CPL of $P_{o(max)} = 1kW$ was clearly identified as an unstable system. Open-loop instability with CPL was studied in asynchronous and synchronous operating modes, identifying different behaviors. As could be observed in the experimental results, this last operating mode caused the oscillations of the state variables to grow without boundaries, creating a highly destructive operating scenario that required shutdown action for protection.

Chapter 3

High Performance CSS-Based Control for CPL Stabilization

3.1 CSS-Based Control Strategy

This section presents the derivation of the Circular Switching Surfaces (CSS) which are later employed to define the closed-loop control law for both operating modes.

3.1.1 CSS Derivation

To derive the switching surfaces, the normalized differential system (2.2) is solved to obtain the converter's circular trajectories for all three of its structures depicted in Fig. 2.2. The differential equations of the system, repeated in (3.1), are combined and solved, obtaining the time domain solutions (3.2) and (3.3).

$$\begin{aligned} \frac{1}{2\pi}\frac{di_{Ln}}{dt_n} &= u_1\ v_{ccn} - u_2\ v_{on} \\ \frac{1}{2\pi}\frac{dv_{on}}{dt_n} &= u_2\ i_{Ln} - i_{on} \end{aligned} \tag{3.1}$$

$$v_{on} = [v_{on}(0) - \frac{u_1}{u_2}\ v_{ccn}]\ cos(2\pi t_n) + [u_2\ i_{Ln}(0) - i_{on}]\ sin(2\pi t_n) + \frac{u_1}{u_2}\ v_{ccn} \tag{3.2}$$

$$i_{Ln} = [i_{Ln}(0) - \frac{1}{u_2}\ i_{on}]\ cos(2\pi t_n) + [u_1\ v_{on}(0) - u_2\ v_{ccn}]\ sin(2\pi t_n) + \frac{1}{u_2}\ i_{on} \tag{3.3}$$

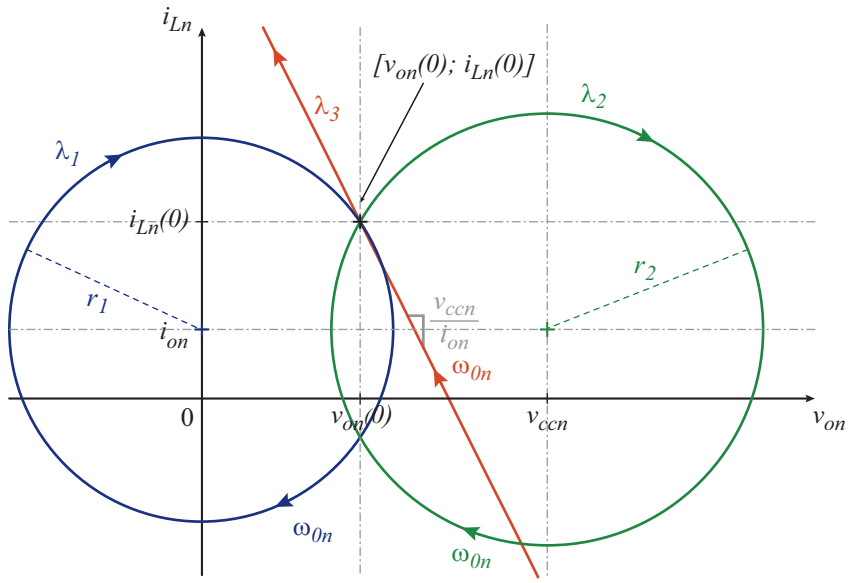

Figure 3.1: Buck+Boost cascade converter trajectories in its three structures describe circumferences in the state plane.

Combining (3.2) and (3.3), time is eliminated, resulting in the generalized trajectory equation (3.4):

$$\lambda : (v_{on} - \frac{u_1}{u_2}\, v_{ccn})^2 + (u_2\, i_{Ln} - i_{on})^2 - [v_{on}(0) - \frac{u_1}{u_2}\, v_{ccn}]^2 - [u_2\, i_{Ln}(0) - i_{on}]^2 = 0 \quad (3.4)$$

Replacing the parameters u_1 and u_2, the trajectories corresponding to each of the structures depicted in Fig. 2.2 are obtained and shown in (3.5) to (3.7).

$$\lambda_1 : v_{on}^2 + (i_{Ln} - i_{on})^2 - v_{on}^2(0) - [i_{Ln}(0) - i_{on}]^2 = 0 \quad (3.5)$$

$$\lambda_2 : (v_{on} - v_{ccn})^2 + (i_{Ln} - i_{on})^2 - [v_{on}(0) - v_{ccn}]^2 - [i_{Ln}(0) - i_{on}]^2 = 0 \quad (3.6)$$

$$\lambda_3 : \left(\frac{v_{ccn}}{i_{on}}\right) v_{on} + i_{Ln} - \left(i_{Ln}(0) + \frac{v_{on}(0)\, v_{ccn}}{i_{on}}\right) = 0 \quad (3.7)$$

These trajectories can be rewritten in the following form:

$$\lambda : (x - C_x)^2 + (y - C_y)^2 - r_o^2 = 0 \tag{3.8}$$

where the center of the circumferences is displaced by v_{ccn} and i_{on}, and the radius r_o depends on the operating point values $v_{on}(0)$ and $i_{Ln}(0)$. To facilitate visualization, the trajectories λ_1 to λ_3 are illustrated in Fig. 3.1 for a particular set of parameters $(v_{on}(0), i_{Ln}(0))$. The direction of the rotational speed ω_{0n} is indicated by a set of arrows on each trajectory. λ_3 is considered a particular case of a circumference in which the center shifts $(C_x, C_y) \rightarrow (\infty, \infty)$ approaching a straight line in the state plane.

3.1.2 Closed-Loop Control Law Definition

The trajectories λ_1 to λ_3, defined in the previous section, are employed to define the control law based on the operating point and the intersection of the converter's switching surfaces. For this task, some parameters need to be defined. $v_{ccn} = 1$, given that the normalization is done with v_{cc}. $v_{on}(0)$ taking values in an interval $(a < v_{on,target} < b)$, depending on the battery SOC. The boundaries a and b are given by the maximum and minimum operating values of the energy storage system. The parameter $i_{Ln}(0)$ is matched with the targeted inductor current $(i_{Ln,target})$ for each operating mode. For step-down operation, since structure I and II are used, $i_{Ln,target} = i_{on}$. For step-up, structures II and III are used, hence i_{Ln} is equal to the input current of the converter and related to the output current i_{on} as $i_{Ln,target} = i_{on}/(1-D)$ with $D = 1 - v_{ccn}/v_{on,target}$. Having all the required parameters defined, the control law is presented for each operating mode.

For step-down operation, $u_2 = 1$ and the control law derived is as follows:

Case I: $(i_{Ln} > i_{on})$

if $(\sigma_1 > 0)$ then $u_1 = 0$, else $u_1 = 1$

Case II: $(i_{Ln} < i_{on})$

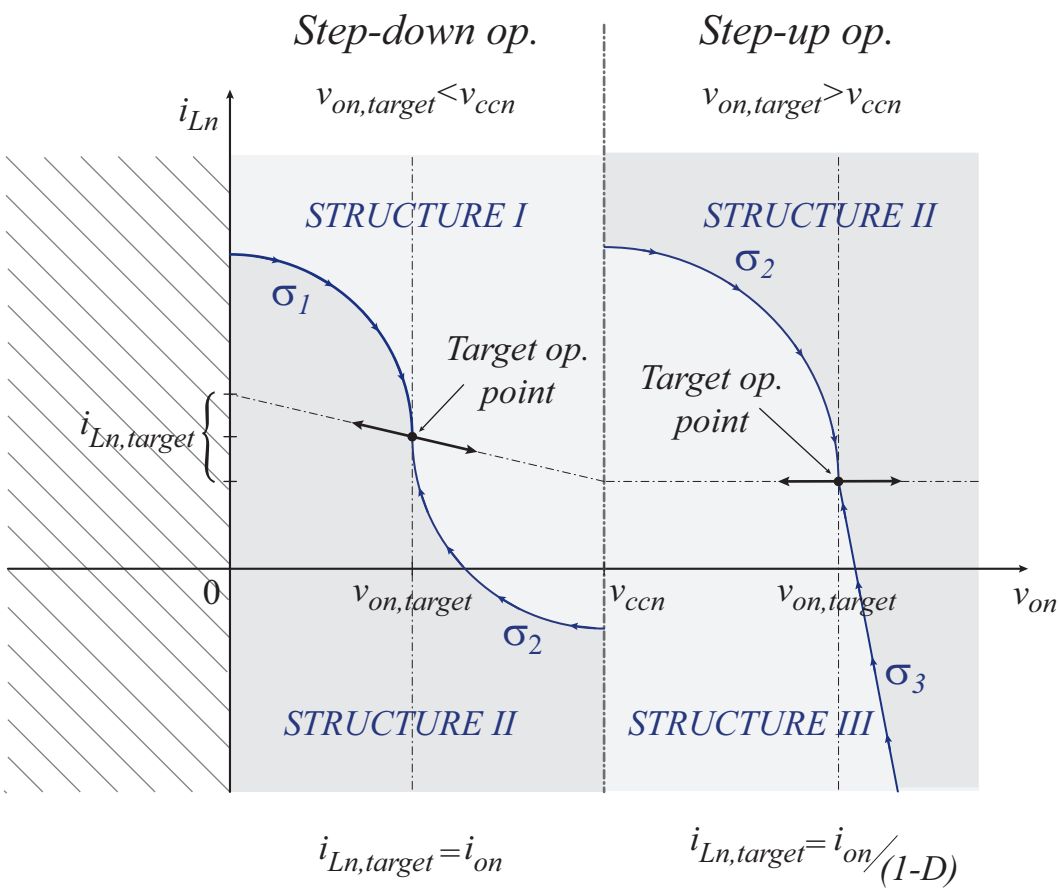

Figure 3.2: For closed-loop operation, switching surfaces σ_1 and σ_2 are employed for step-down operation, while σ_2 and σ_3 are used for step-up operation.

if $(\sigma_2 > 0)$ then $u_1 = 1$, else $u_1 = 0$

where

$$\sigma_1 : v_{on}^2 + (i_{Ln} - i_{on})^2 - V_{on,target}^2 \tag{3.9}$$

$$\sigma_2 : (v_{on} - v_{ccn})^2 + (i_{Ln} - i_{on})^2 - (V_{on,target} - 1)^2 \tag{3.10}$$

In step-up operation, $u_1 = 1$ and the control law is defined as follows:

Case I: $(i_{Ln} > i_{on}/(1 - D))$

if $(\sigma_2 > 0)$ then $u_2 = 1$, else $u_2 = 0$

Case II: $(i_{Ln} < i_{on}/(1 - D))$

if $(\sigma_3 < 0)$ then $u_2 = 0$, else $u_2 = 1$

where

$$\sigma_2 : (v_{on} - v_{ccn})^2 + (i_{Ln} - i_{on})^2 - (V_{on,target} - 1)^2 - (i_{on}\, V_{on,target} - i_{on})^2 \tag{3.11}$$

$$\sigma_3 : \left(\frac{1}{i_{on}}\right) v_{on} + i_{Ln} - \left(V_{on,target}\, i_{on} + \frac{V_{on,target}}{i_{on}}\right) \tag{3.12}$$

Fig. 3.2 illustrates the control laws with the CSS established, showing the two areas of operation which are determined based on the dynamic value v_{on} with respect to v_{ccn}.

To understand the operation and gain insight into the behavior of the CSS-based control strategy proposed, Fig. 3.3 presents the analysis of the CSS with the converter trajectories loaded with CPL for each structure depicted in Fig. 2.2. The points A shown in the subfigures correspond to different initial conditions (ICs) for which the CSS have a sufficiently small error regarding the CPL trajectory, ensuring that the target can be achieved by switching to the corresponding structure indicated as λ_{x_target}. This condition is satisfied for all ICs that are in the region between the curve P_{on} and a certain limit, which is determined by the maximum output voltage ripple, e.g. 2%. Thus, when the CSS represented as λ_{x_target} within

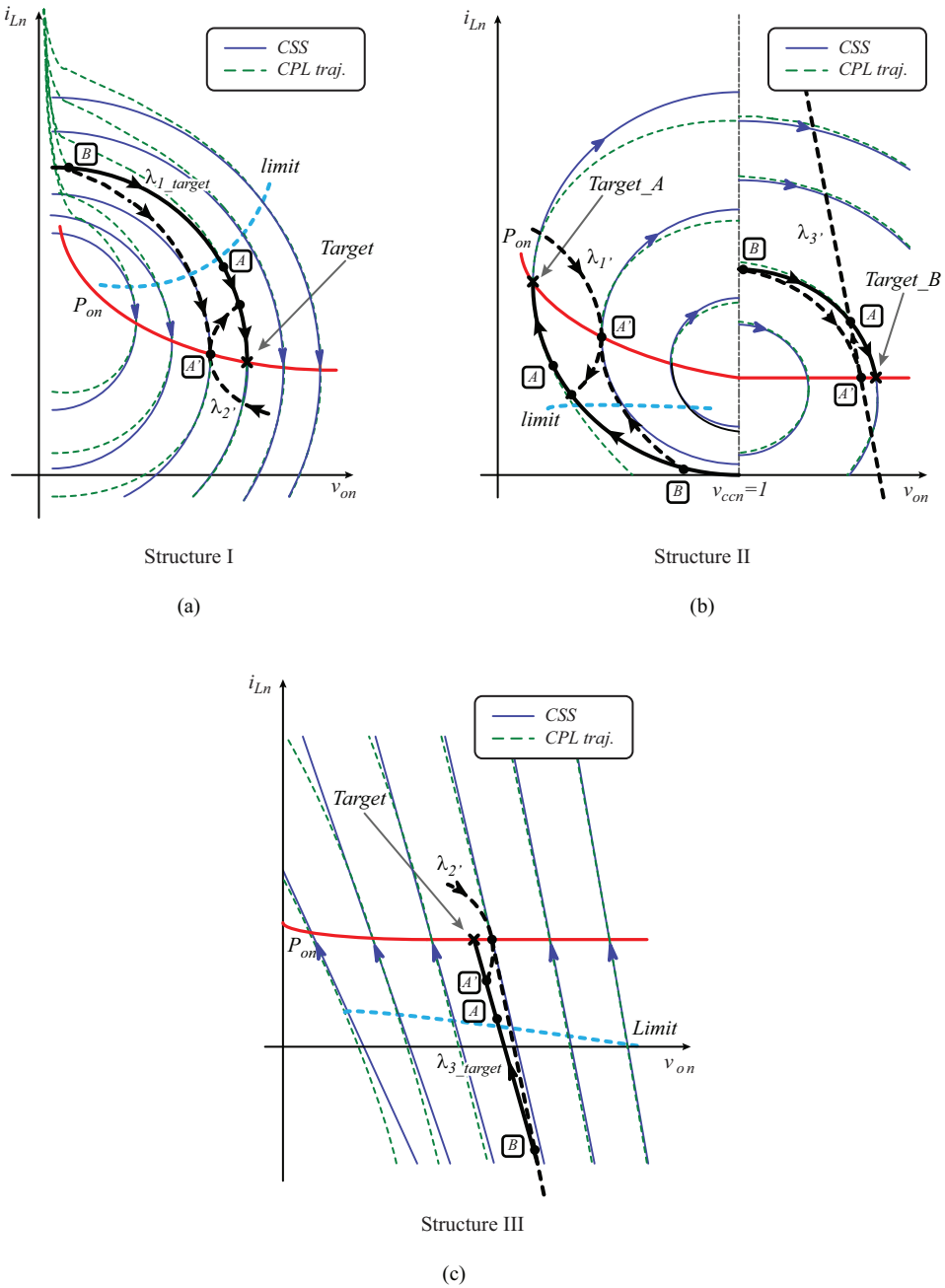

Figure 3.3: The CSS-based control strategy is conceptually analyzed in the state plane with the CPL trajectories. For the converter in its three structures, a wide operating area is identified for stable operation and optimal transient response.

the given region is selected, the trajectories evolve until the condition $v_{0n} \pm 2\%$, achieving steady state.

For points B outside the region where the CSS trajectory matched the target CPL trajectory, the circles that describe the target CSS trajectory now match different CPL trajectories that intersect the p_{on} line at a v_{on} value which can be either higher or lower than $v_{on} = V_{on,target}$ (Point A in Fig. 3.3). However, it can be demonstrated that the operating point is always able to return to the convergence area by switching to the proper structure as is indicated conceptually in Fig. 3.3 for the different cases. Consequently, once point A is reached, the structure is switched according to the operating mode, reaching again the target CSS trajectory that allows the operating point to arrive at the desired target. Although extra switching actions are required, the operating region is extended.

3.2 Closed-Loop Operation and Performance Assessment

The CSS were implemented in simulation for the Buck+Boost cascade converter for start-up and CP loading transients. Results are shown in Fig. 3.4(a) and (b) for step-down and step-up operation, respectively.

In the first case, the converter is initially driven from ❶ to the target point with no load ❸. With the switches configured as in structure II, the operating point moves along λ_2. When it reaches the switching surface $\sigma_{1(P_{on}=0)}$ ❷, the converter switches to structure I, achieving steady-state in two switching actions in minimum time. At instant $t_n = 1$, a CPL of $P_{on} = 0.15$ is applied and the new target point moves to ❺. According to the CSS, the converter switches again to structure II until it reaches the switching surface $\sigma_{1(P_{on}=0.15)}$, where the control now switches back to structure I. The operating point is directed towards the target, where it achieves steady state. The same start-up and loading process is done for step-up operation and shown in Fig. 3.4(b). In this case, the controller uses structures

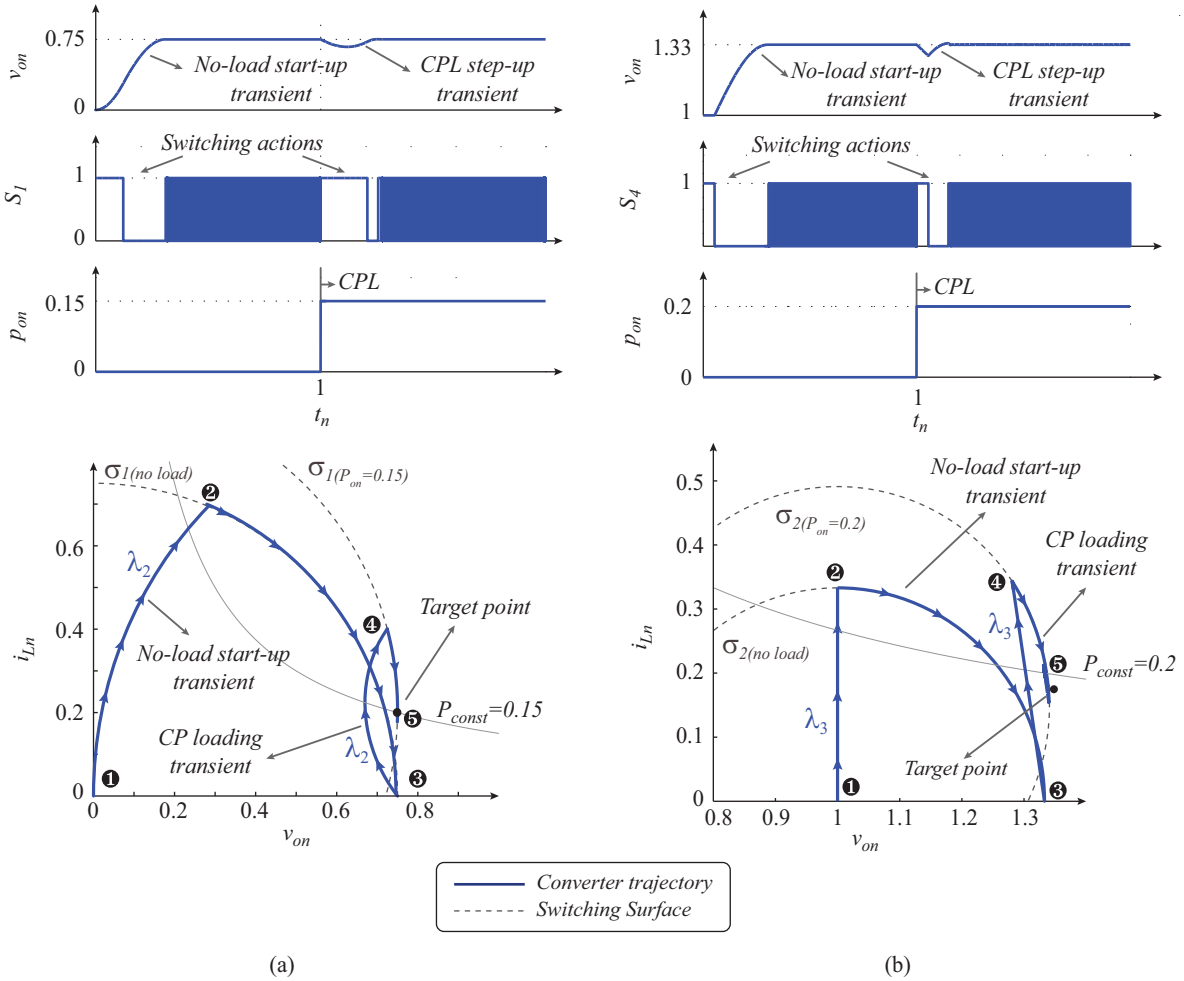

(a) (b)

Figure 3.4: Closed-loop operation using the CSS for (a) step-down and (b) step-up operation. The controller addresses time-optimal start-up and stable operation with near-optimal transient response for sudden load changes.

II and III to drive the operating point towards the target with CPL of $P_{on} = 0.2$. These results show the stabilizing capabilities and enhanced transient responses for the CSS with sudden load changes in both operating modes.

Important advantages in terms of performance and switching actions are obtained when driving the operating point towards the target point through near-optimal trajectories. A comparison between the closed-loop control implementing the CSS with linear compensated control and sliding-mode control (SMC) is shown in Fig. 3.5. Time domain and state-plane

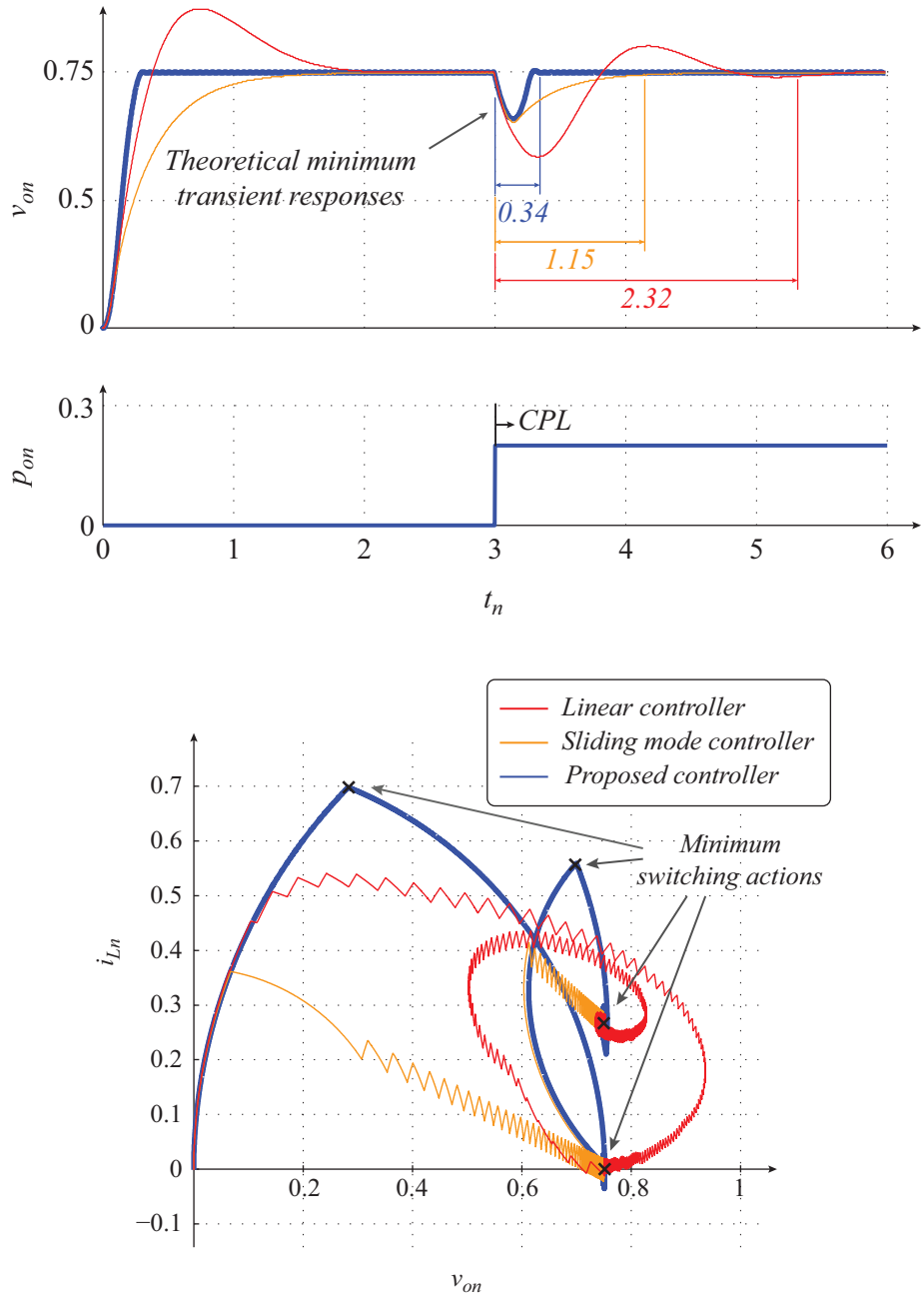

Figure 3.5: Simulation results for the proposed closed-loop control based on the CSS shows an important time-recovery improvement with reduced switching actions when compared with linear compensated control and SMC.

plots show start-up and sudden load change transient performance for the three control techniques. The linear controller was implemented in a compensated converter with the

traditional approach, by analyzing root locus and frequency response for the design of the feedback loop. Analyzing the response of the converter to a sudden CPL change, it is observed that the converter achieves stability after 2.32 normalized time units. SMC is an interesting alternative control for stabilizing and controlling CPL systems. For this controller, a transient of 1.15 normalized time units is obtained for the same load change. With the CSS-based control, the recovery time shown for the same CPL step is 0.34 normalized time units, representing an improvement of 3.4 times with respect to SMC and of 6.8 times with respect to the linear controller. Analyzing the switching actions (in the state-plane plot) required by each technique to arrive at the new target point after the sudden CPL change, it is observed that the proposed controller implements only two switching actions, while for the other two techniques, the number is extremely large.

3.3 Stability and Limits of Operation

Several approaches can be found in literature to analyze the stabilization capabilities of the proposed control technique. Middlebrook's criterion [40], derived from the impedance ratio analysis in filtered switching power converters has been found quite conservative. Nevertheless, combined with gain- and phase-margin criteria, this analysis can deliver good insight into the stabilization characteristics of the controlled converter.

Power converters applied to traction systems might have limited response capabilities to ensure smooth operation, especially in vehicle applications. On the other hand, cascaded converters such as step-down converters for powering low-power loads present increased bandwidth. Fig 3.6 shows the output impedance Z_{source} of the cascade converter in closed-loop operation overlapped with the input impedance Z_{load} of two CPL cases. One case considers a high-bandwidth CPL which was employed for the experimental section, while the other one has limited dynamic bandwidth, approaching a more realistic case.

Impedance ratio criterion requires $Z_{source} << Z_{load}$, which in practice can be extended

to $-6dB$ difference to ensure stable operation. In this condition, a phase margin of 50 is acceptable for stability. As shown in the Bode plot in Fig 3.6, CPLs exhibit a negative impedance characteristic $Z_{load(highBW)}$ and $Z_{load(lowBW)}$. In the case of the high-bandwidth CPL, this behavior is maintained up to a frequency of $25kHz$, at which point the gain starts to increase, reducing the instability effects. Variation on the phase also indicates that the behavior is no longer pure CP. For the limited bandwidth CPL, the bandwidth goes down to $1kHz$. The cascade converter loaded with $P_o(max) = 1kW$, on the other hand, presents a desirable reduced output impedance for a wide bandwidth, enough to ensure steady-state operation in both CPL cases.

In terms of transient response, the analysis and results presented in the previous section are extended to different operating points along the CP curve, as well as implemented with different CPL steps to characterize the behavior of the proposed controller. Fig. 3.7 presents the simulation results for the Buck+Boost cascade converter in step-down and step-up operating mode for a family of CPL steps. Under the operating conditions indicated in the figure, successive CPLs are applied in steps of $\Delta P_{on} = 0.05$. Curves obtained for the simulation indicate that the controller is able to stabilize CPL steps of up to $P_{on} = 0.25$ for both operating modes, exhibiting less than 5% overshoot. These results define an improved dynamic performance over an important set of working conditions, making the technique widely applicable for CPL stabilization and loading transient control.

The sensitivity of the control technique regarding filter parameter drifting and tolerances was also examined. Different scenarios were established for the normalization procedure applied in Chapter 2, Section 2.2, focusing on the filter characteristic impedance $Z_o = \sqrt{L/C}$. The worst case occurs when the value of L or C increases while the remaining parameter equally decreases. The filter parameters were subject to a variation of 10%. The effect of such variations is a transformation in the switching surfaces, which become elliptical rather than circular. Simulations were developed for the different cases so that the response variations could be analyzed. The distortion of the switching surfaces affected the evolution of

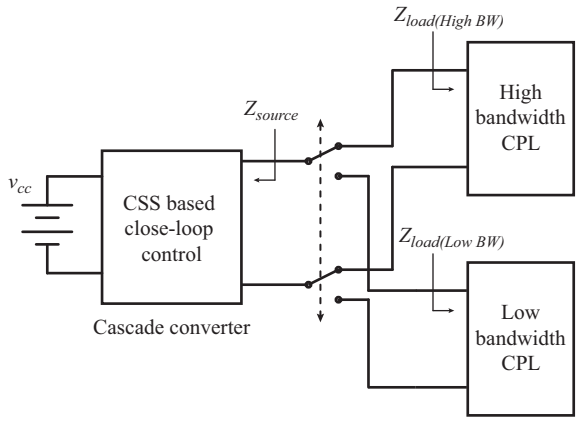

(a)

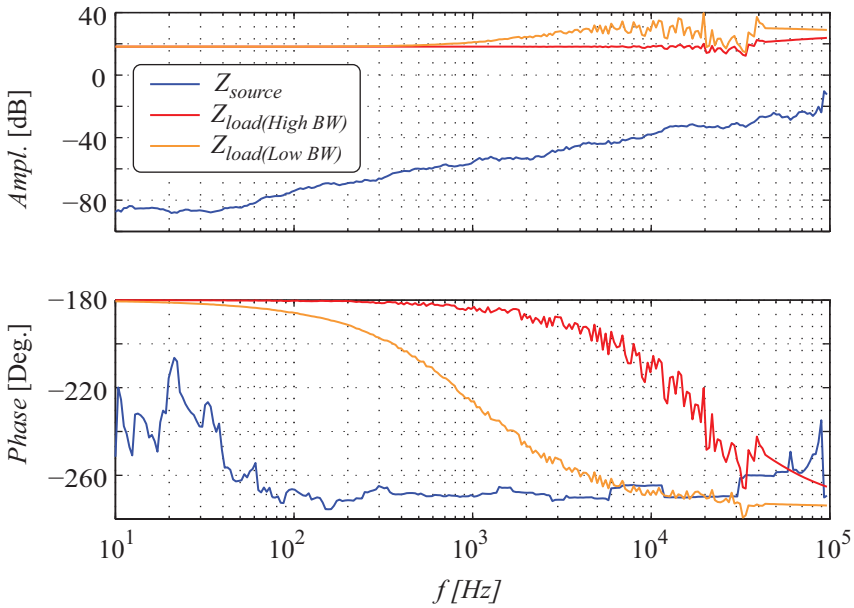

(b)

Figure 3.6: Impedance analysis results for the structure (a) shown in (b) reveal a highly reduced Z_{source} for the cascade converter compared with the Z_{load} of the CPLs, confirming the stabilization capabilities of the proposed control technique.

the operating point during a sudden load change and showed less than 5% overshoot compared with the ideal case under the same operating conditions. Regarding steady state, the variations observed were negligible. Moreover, by applying precise calibration, the distortion effect due to parameter variation can be minimized.

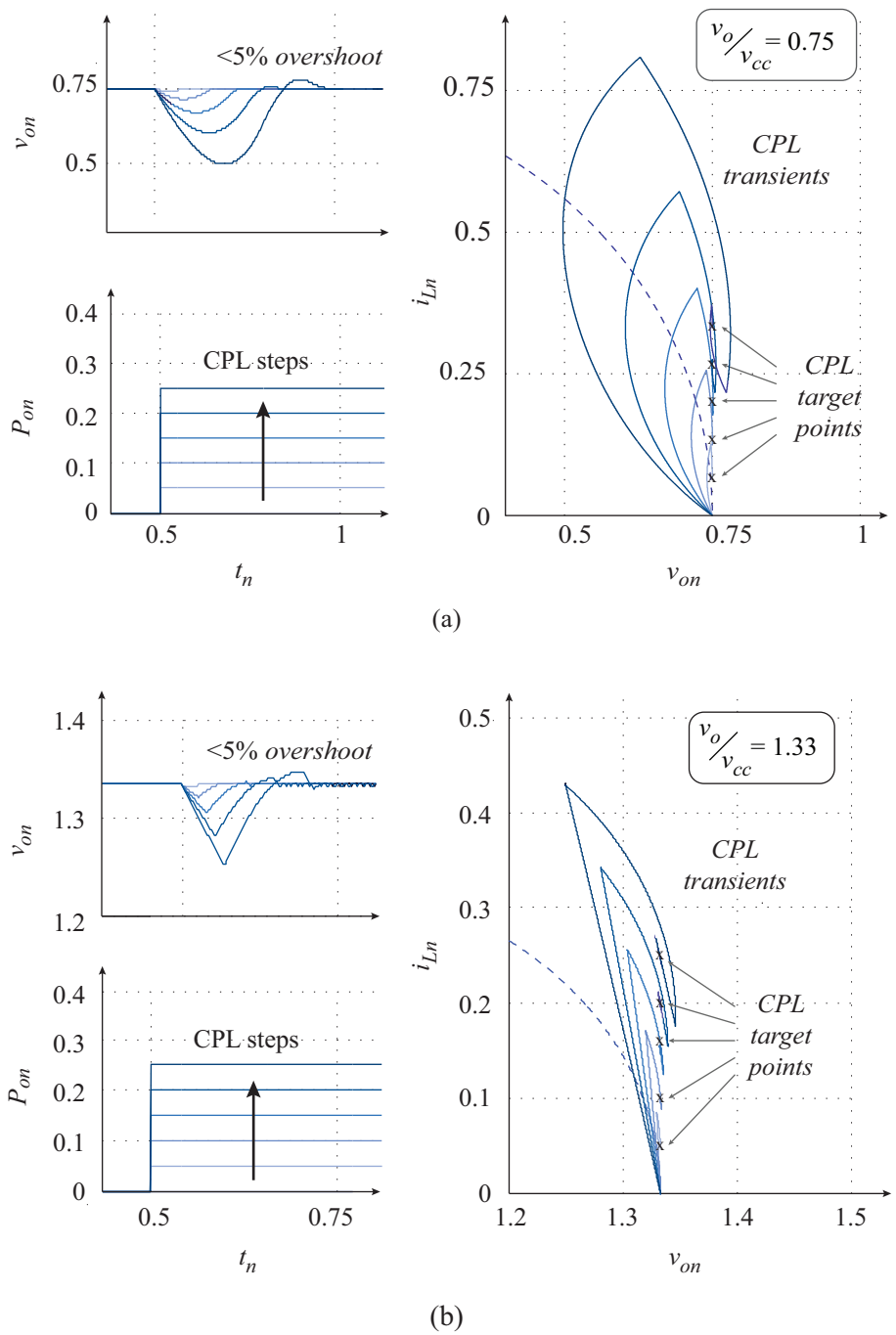

Figure 3.7: Transient response for a family of CPL steps in (a) step-down and (b) step-up operation shows transient response improvements for several loading conditions.

3.4 Experimental Results

Experimental tests were done in the platform described in Chapter 2, Section 2.4, which was designed with a $20\mu F$ metal-film output capacitor. This reduced output capacitance leads to open-loop unstable behavior.

Open-loop instability produced by the CPL was shown in Figs. 2.5 and 2.6, where the converter was operating in step-down mode at a fixed switching frequency and constant duty-cycle. The load is initially resistive, dissipating $P_o = 250W$. The response at the output of the converter after switching to CPL at $t_1 = 3.2ms$ exhibits oscillatory behavior at the resonance frequency $f_o = 1.15kHz$. Synchronous operation (Fig. 2.6) was identified as the worst case operating condition, since oscillation grew without boundaries. For protection, output voltage and current thresholds are set to shut down the power stage to avoid a catastrophic failure. If asynchronous switching were to be implemented, operation would be restricted to the first quadrant, thus enabling operation in DCM. In this case, instability effects are reduced by preventing inductor current i_{Ln} from reversing direction and forcing the trajectory to follow the normalized output voltage axis as shown in Fig. 2.5.

To stabilize the open-loop converter, a $1.1mF$ electrolytic capacitor would be required. Besides the increased capacitance, this type of technology presents an ESR approximately 10 times larger than the ESR of the metal-film type employed, which has significant impact on the filter losses. Additional advantages are the extended lifetime for reliable operation and reduced volume and mass. A detailed comparison is provided in Table 3.1.

The proposed CSS was implemented in order to control the unbounded behavior and obtain predictable, stable operation. Experimental results for the converter operating under the CSS-based control strategy are shown in Figs. 3.8 to 3.11. In all cases, the experimental results closely resembled the simulation results.

Stabilization of the system under CPL load is shown in Fig. 3.8, where the converter is loaded with a $P_o = 400W$ CPL. In the first half of the oscilloscope capture, the converter is operating in open loop and exhibits bounded oscillation. The demonstration of the unstable

PARAMETER	Film (MKP1848620704P4)	Electrolytic (CGS112T500V4L)
$Capacitance$	$20\mu F$	$1100\mu F$
$R_C(ESR)$	$9m\Omega$	$92m\Omega$
$Dimensions$	$43.00mm\ x\ 21.50mm$	$50.80mm(\varnothing)$
$Volume$	$36.6mm^3$	$238.1mm^3$
$Mass$	$36g$	$250g$
$Lifetime$ (@ 85°)	$100,000hs$	$2,000hs$
$Price(qty\ 50)$ (2014)	\$11.20	\$85.01

Table 3.1: Output capacitor comparison

behavior is done in asynchronous mode to limit the amplitude of these oscillations. In the second half of the oscilloscope capture, the proposed CSS strategy is enabled, resulting in stable operation. Note that the controller only performs two switching actions (structures I and II) to drive the operating point towards the target point where it remains stable.

In Fig. 3.9, the converter's stability is further tested by loading the converter with $P_o(max) = 1kW$. The converter exhibits stable operation with a switching frequency of $f_{sw} = 8KHz$, which is accomplished by employing an hysteresis band in the CSS control laws to obtain the desired ripple. As for frequency shifting, a narrow variation is observed in steady-state operation. If necessary, this variation can be further mitigated by adjusting the hysteresis band control in the CSS or forcing PWM triggering with precision timers.

Experimental results for transient response to sudden CPL change were shown in Fig. 3.10 for step-down and step-up operating modes. State-plane plots on the right-hand side of each experimental capture expose the evolution of the operating point through near optimal trajectories, from no-load steady state to a $500W$ CP loading condition. Unloading to a no-load condition for both cases yielded the same results in terms of transient recovery.

Further experimental results to evaluate the predicted transient response are shown in Figs. 3.11(a) and (b), where a family sudden CPL step changes is applied to the converter. In Fig. 3.11(a), the cascade converter is operating in step-down mode with $V_o/V_{cc} = 0.75$. At $90V$, the CPL step-ups are applied. In each case the control strategy responds by changing

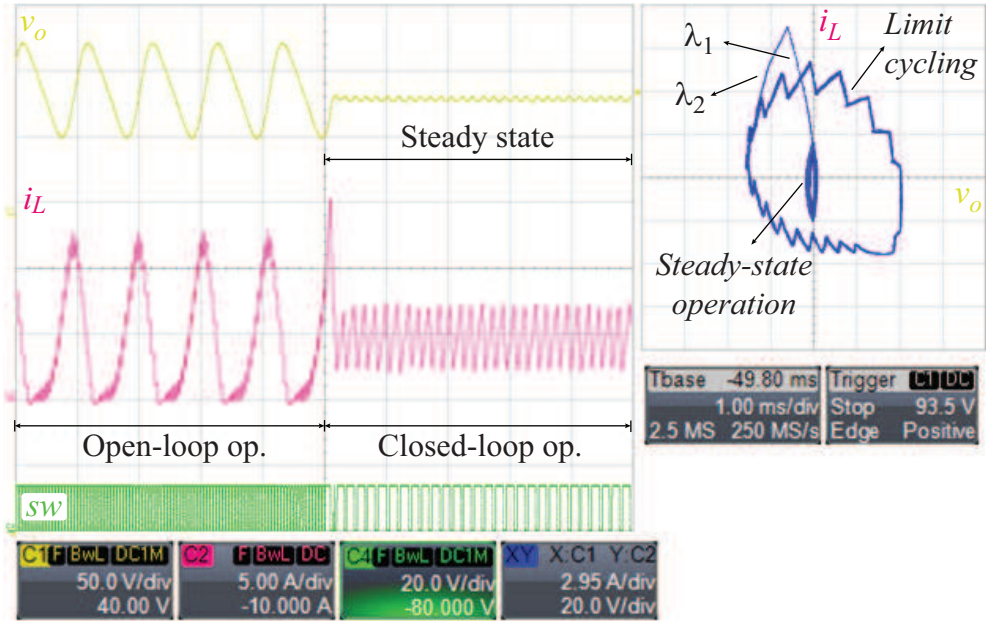

Figure 3.8: Experimental results for output stability obtained for the converter loaded with $400W$ CPL when operation is switched from open loop to closed loop with CCS.

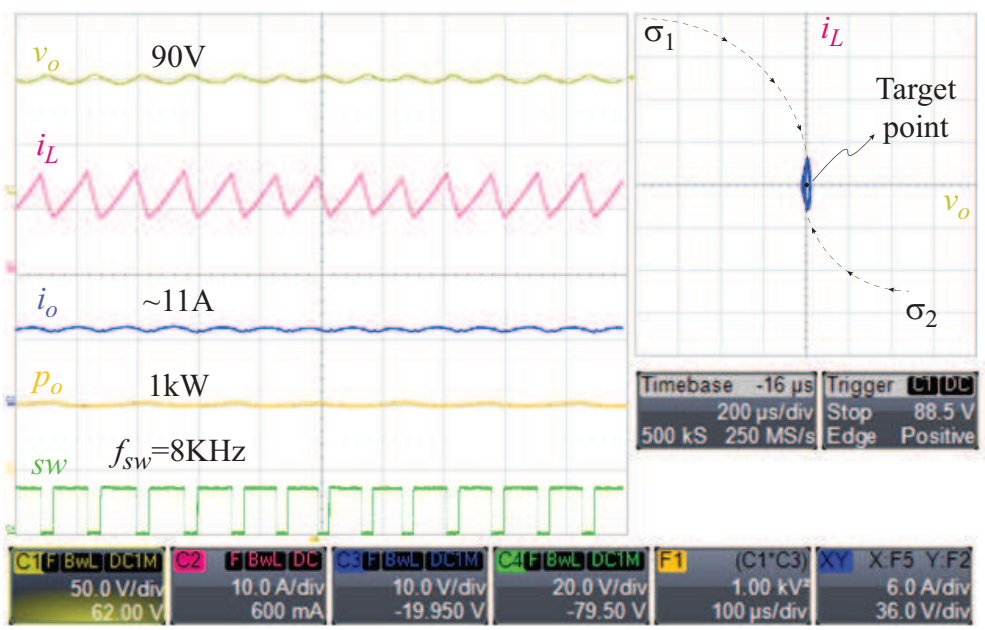

Figure 3.9: Experimental results for the cascade converter loaded with $1kW$ CPL in closed-loop step-down operation.

the converter structures according to the CSS control law, achieving fast recovery to steady-state. The results exhibit an output voltage overshoot of less than 5% for CPLs up to

$P_o(max) = 500W$ as was predicted in section VI. Fig. 3.11(b) shows near-optimal response for a sudden CPL load change with negligible overshoot for the cascade converter operating at $V_o/V_{cc} = 1.25$ (step-up operation).

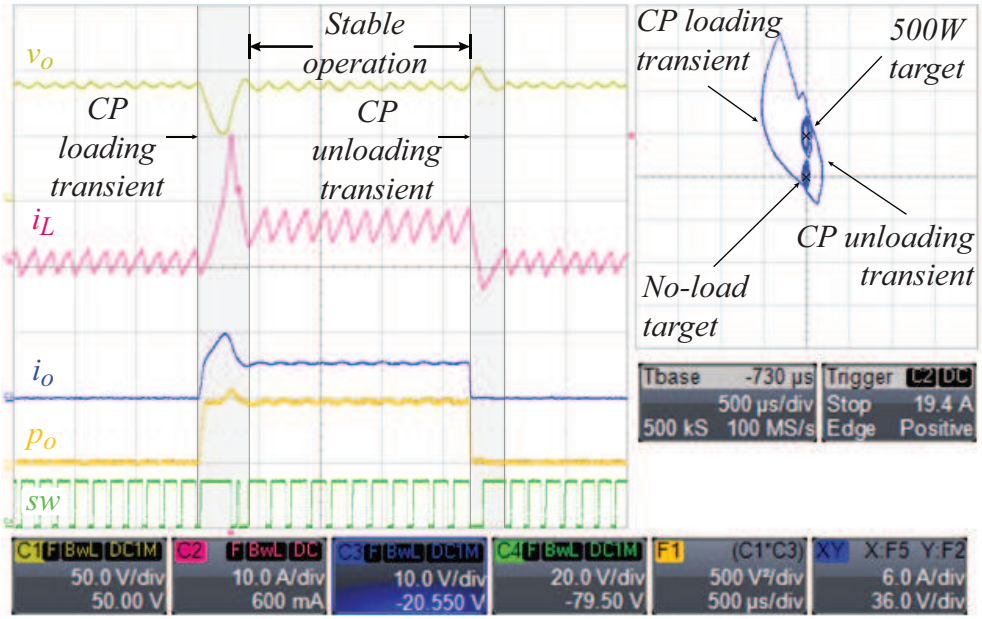

(a)

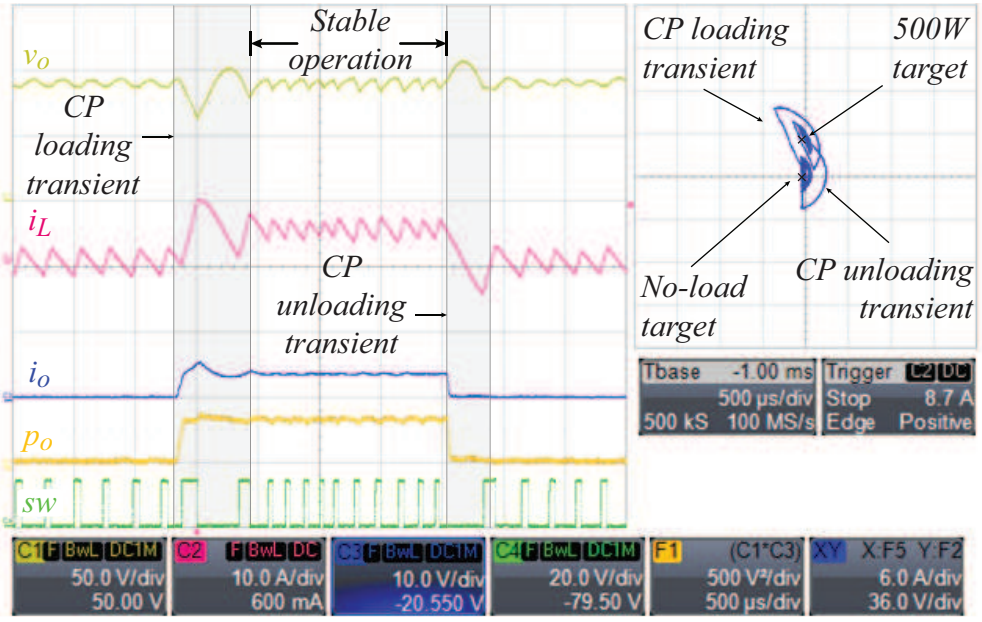

(b)

Figure 3.10: Experimental results for the $1kW$ platform in (a) step-down and (b) step-up operation for a $500W$ CPL loading and unloading transients show the near-optimal operation with the CSS control strategy.

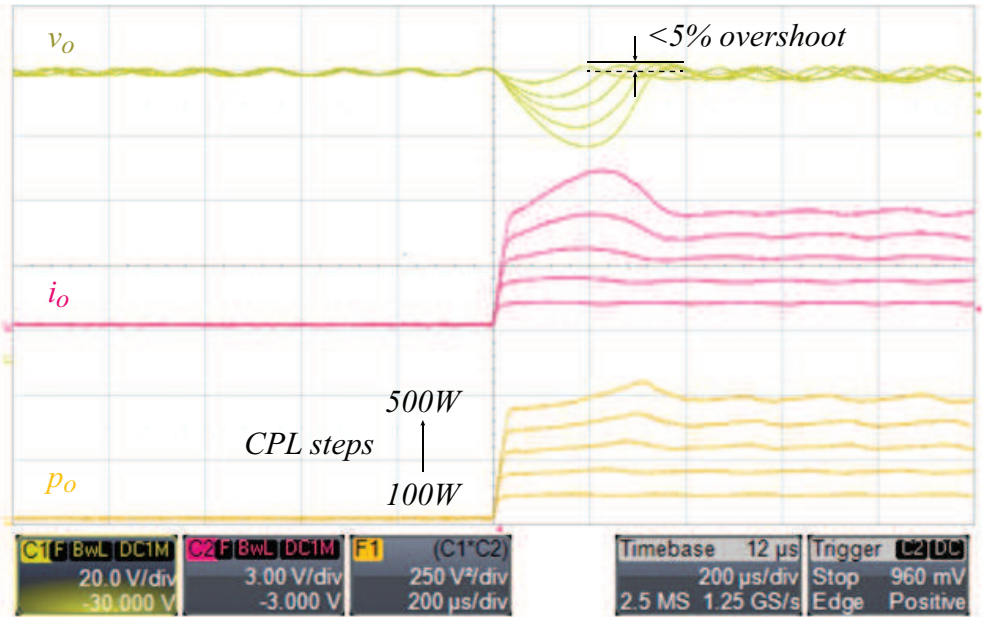

(a)

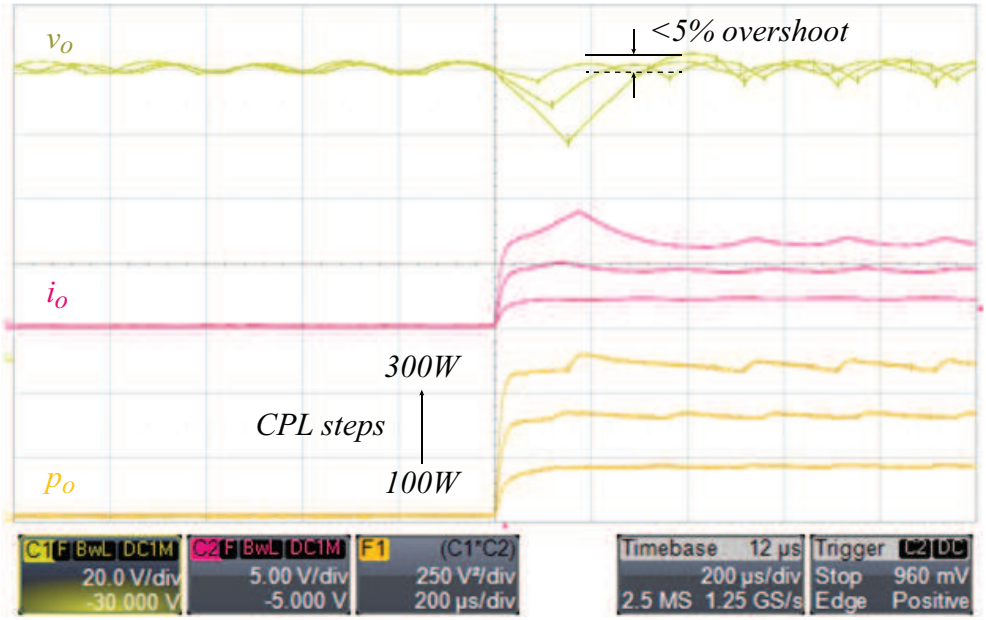

(b)

Figure 3.11: Experimental results for the $1kW$ platform in (a) step-down and (b) step-up operation for several CPL steps show improved dynamic output response with minimum overshoot.

3.5 Summary

This chapter presented the derivation and implementation of the CSS-based control technique for CPL stabilization. Closed-loop operation was analyzed with a simulation and validated through experimental results in the scaled $1kW$ Buck+Boost cascade converter. Operation of the proposed control technique was conceptually analyzed in the state plane, comparing the CSS and the CPL trajectories of the converter in its three structures and identifying a wide operating area for stable operation and optimal transient response.

Impedance analysis of the converter showed reduced output source impedance, indicating extremely high dynamic capabilities and avoiding the use of bulky DC capacitors for bus stabilization. This allows for the usage of metal-film capacitors, which have reliability advantages over commonly employed electrolytic capacitors as well as reduced ESR, improving system efficiency.

Besides the stabilization characteristics of the controller proposed, comparison with a traditional compensated linear controller and a non-linear SMC showed significant improvements in terms of dynamic response for sudden CPL changes.

The analysis was done in a normalized converter, allowing the results to be extrapolate to any platform by denormalization according to the specifications and requirements of a given converter.

Chapter 4

Development of High-Power Motor Drive Platform for Electric Vehicles

Effective motor drive control for vehicle propulsion requires implementation of elaborated controlled power structures to manage power flow in an accurate and reliable manner. For motor drive operation, DC energy is delivered to the electric motor through a 3-phase inverter structure controlled by a speed/torque control. A precise control is required to ensure smooth operation of the motor. Meanwhile, during regeneration process, mechanical energy stored in the electric motor is converted to electrical energy and returned to the electric system. Effective energy management is required to ensure safe operation and avoid high DC voltage levels in the bus.

In terms of efficiency, it would be desirable to recover and store the total mechanical energy available from the drive train in the batteries for later usage. However, given the energy storage capability, if the battery state-of-charge (SOC) is high, energy has to be managed in another way. Dynamic Braking uses a high-power shunt regulator across the DC bus to dissipate the extra energy, resisting rotation, and decreasing motor speed.

4.1 System Requirements

In order to achieve comprehensive and accurate bidirectional power flow control, a high-power motor drive platform is required. The following are the key characteristics and capabilities achieved in the power stage designed:

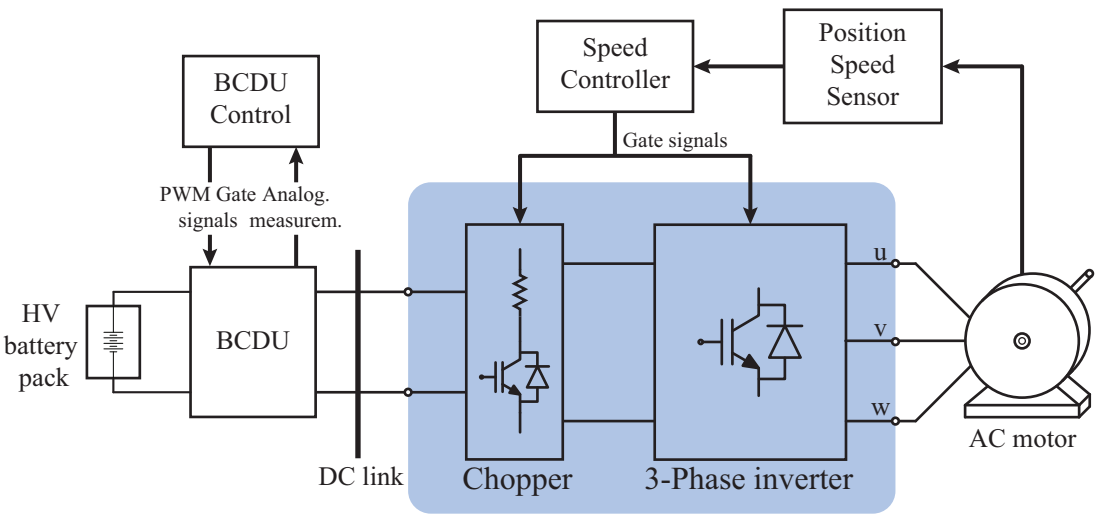

Figure 4.1: Block diagram of the high-power motor drive platform.

- Multipurpose and flexible platform, allowing for adaptation to different needs in terms of motor driving, measurements and sensor connectivity.
- Hardware robustness able to withstand mechanical stress and EMI.
- Capable of handling $20kW$ of peak power flow within a $400VDC$ system.
- The power stage must be able to operate at a switching frequency of $f_{sw} = 10kHz$ with an output frequency of $f_o = 400Hz$.
- 3-phase voltage and current measurements.
- Temperature sensing.

4.2 Platform Description

Figure 4.1 presents the block diagram of the Power Drive Platform.

4.2.1 Power Module

The Power stage is designed to work with Intelligent Power Modules (IPM) from Powerex. The heart of the power platform is the Powerex IPM $PM300RL1A060$, which is an isolated-

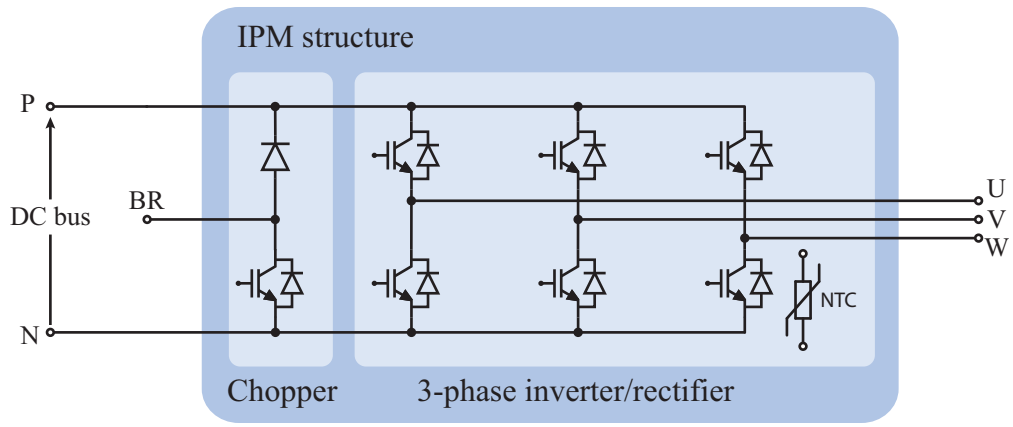

Figure 4.2: Schematic diagram of the high-power IPM.

base module designed for power switching applications operating at frequencies of up to $f_{sw} = 20kHz$. Voltage and current rating of the chosen power module exceed power handling requirements, allowing for future application in higher power motor driving.

The IPM 7-pack structure is shown in Fig. 4.2 and consists of a 3-phase inverter complemented with a chopper structure for dynamic braking.

7-pack module features:

- Embedded Gate Drive Circuit.
- Protection Logic with Fault-Operation output signal.
- Short-Circuit detection (SCD).
- Over-Temperature Detection (OTD) using On-Chip Temperature Sensing.
- Under-Voltage Detection (UVD).
- Low losses level.

The advantages presented by this module are the built-in control circuits which provide optimal gate drive for the switches, improving overall performance in terms of efficiency and protection for the IGBTs and free-wheeling diodes. The combined integrated structure inverter + chopper allows for full control in most motor drive applications.

IPM parameters	
IGBT Inverter Sector	
Collector-Emitter Voltage (V_{ce})	$600V$
Collector-Emitter Saturation Voltage ($V_{ce(sat)}$)	$1.75V$
Collector Current (I_c)	$300A$
Peak Collector Current (I_{cp})	$600A$
Diode Forward Voltage (V_{ec})	$1,7V$
PWM Input Frequency (f_{sw})	$20kHz$
Collector Dissipation (PC)	$833W$
IGBT Brake Sector	
Collector-Emitter Voltage (V_{ce})	$600V$
Collector Current (I_c)	$150A$
Peak Collector Current (I_{cp})	$300A$
Diode Forward Voltage (I_f)	$150A$
PWM Input Frequency (f_{sw})	$20kHz$
Collector Dissipation (PC)	$520W$

In terms of flexibility, several 6-pack and 7-pack IPM modules with different power rates and the same hardware connection interface are available which can be interchanged and connected to the power board.

Table 4.2.1 presents the main characteristics of the IPM:

4.2.2 Interface Design

To drive the IPM, isolated power sources need to be supplied to each of the gate drive circuits. 3 independent 1.5W DC-DC converters ($VLA106\_24151$) are used to supply the 3 top switches in the inverter. The 4 bottom switches, including the brake chopper, share common ground, which allows for the use of a single 4.5W DC-DC converter ($VLA106\_24154$). VLA606-01R is an interface module for IPM driving which contains isolation optocouplers. A differential line receiver is used in the power driver to convert the differential signals sent from the digital control into single-end signals. An inverting buffer is placed to fix the logic of the circuits and to provide the level of current needed to correctly drive the optodrivers.

– Current measurement: for current measurement the LEM HASS-100S was selected, which provides a primary current measurement range of $300A$. In a 3-phase system with

PARAMETER	VALUE
$Oper.volt.$	$230V$
$Amps_{(NL)}$	$0.9A$
$P_{o(max)}$	$0.25Hp$
$Freq.$	$0 - 60Hz$
$Max\ speed$	$5400RPM$

Table 4.1: AC motor parameters

a floating neutral point only 2-phase currents would be required to be sensed. For safety issues, 3-phase current measurements are set, providing redundancy to the system which allows for the detection of unbalanced and/or faulty operating conditions. Current in the brake switch is also measured to aid in the control of the dynamic braking.

– Voltage measurement: resistive voltage divider for 3-phase and bus voltage was implemented on the power board. This is a cost effective solution which allows voltage measurement in the inverter, providing the proper analog stage in the control board for filtering and signal scaling.

– Temperature measurement: the system has two temperature measurement points. The first is embedded in the power module and is used for the internal protection circuitry. To enable temperature monitoring in the control board, a second sensor based on a $LM35$ is placed in the heat-sink plate. Signal from the sensor is sent to the control board for temperature tracing.

The interface board was designed in Altium Designer and the 3D render is shown in 4.3.

4.2.3 Open-Loop Test

Testing of the high-power platform was done by implementing a scalar Volts-per-Hertz control [41]. This technique provides variable speed control of an AC machine with a simple implementation in open-loop mode. The essence of the technique, which is briefly described below, lies in the regulation of the input phase voltage according to the operating rotating frequency so that the voltage-to-frequency ratio is kept constant. In this way flux linkage is

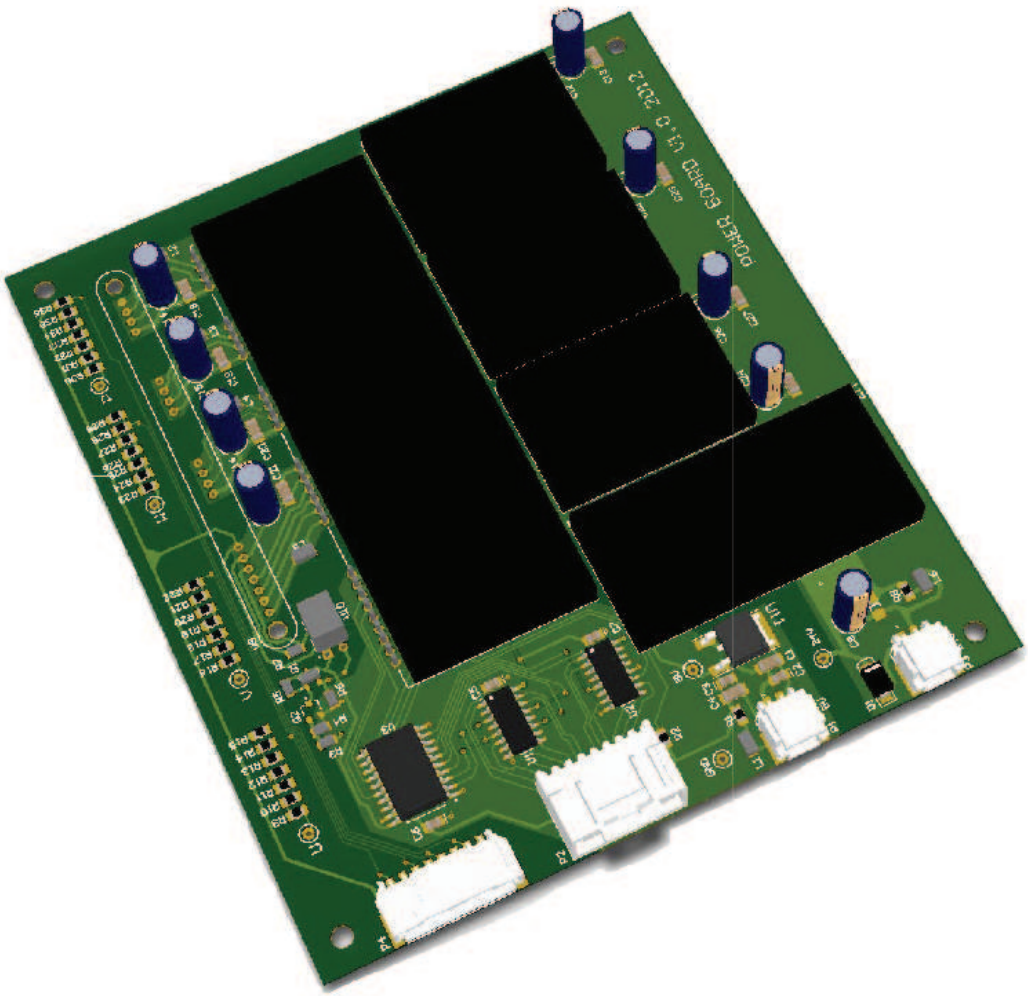

Figure 4.3: 3D design of the IPM interface board.

maintained, avoiding saturation.

If the mechanical system is externally loaded, and does not exceed the nominal torque, the angular speed can be calculated from the supply voltage frequency:

$$\omega_s = \frac{2\pi f_s}{p} \tag{4.1}$$

With $p = num.of poles$ The RMS value of the induced voltage $E_{f,ph}$ is given by the following:

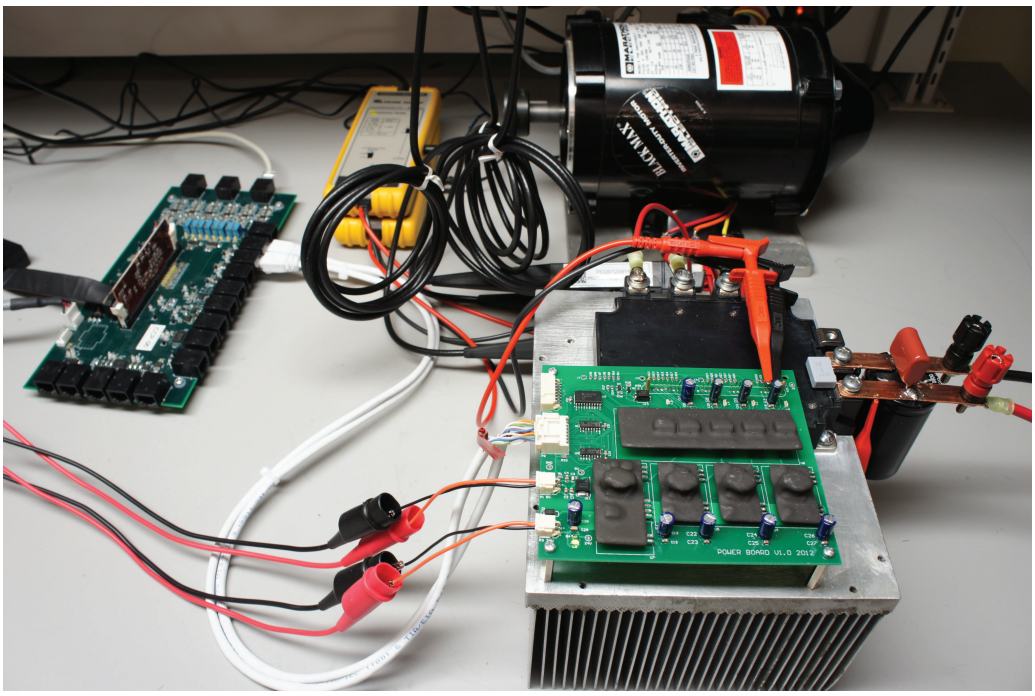

Figure 4.4: Platform test setup.

$$E_{f,ph} = \sqrt{2}\pi f_s N_s k_w \phi \tag{4.2}$$

If the stator resistance is small enough to be neglected, then the stator phase voltage $V_{s,ph}$ is equal to the induced voltage $E_{f,ph}$, and the flux linkage can be approximated as follows:

$$\phi = \frac{V_{s,ph}}{\sqrt{2}\pi f_s N_s k_w} = k\frac{V_{s,ph}}{f_s} \tag{4.3}$$

The control technique was implemented in C28x Delfino MCU to control the AC motor whose characteristics are depicted in Table 4.1. Fig. 4.5 shows the 3-phase current fed to the motor with no load running at $60Hz\frac{120}{4poles} = 1800RPM$ during the platform test. The power platform operated satisfactorily over the tests developed, confirming the interface design.

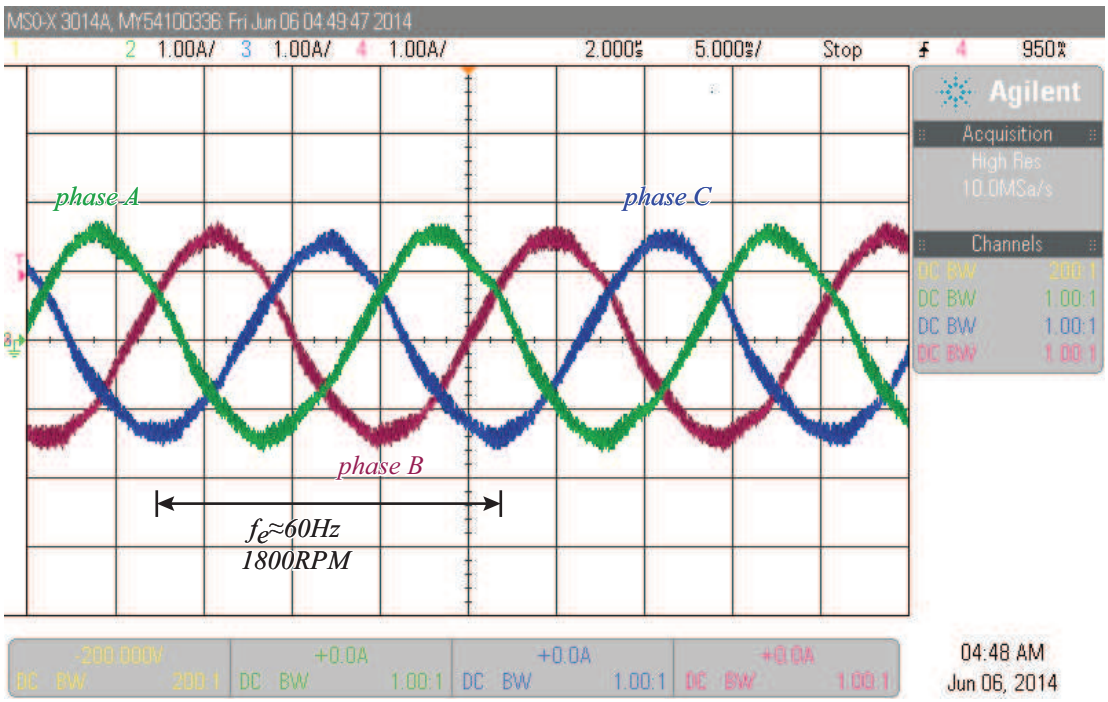

Figure 4.5: Experimental results show the 3-phase stator currents for the 0.25HP AC induction motor with no load running at the nominal speed of 1800RPM.

4.3 Summary

This chapter presented the design, construction and testing of the 3-phase high-power platform for electric motor driving. The platform operates with an Intelligent Power Module (IPM) from Powerex to manage power flow. The board designed to interface with the power module integrates voltage, current and temperature measurements and connects with several IPMs modules, giving flexibility to adapt the power module according to the development. Testing of the platform was done in a $0.5HP$ AC induction motor drive controlled with Voltz-per-Hertz control technique and satisfactory results were obtained.

To provide position/speed sensing a resolver interface was designed composed of a high-current driver to excite the rotor coil and two analog stages for the quadrature stator signals.

Chapter 5

Conclusions

5.1 Summary

This thesis investigated the unstable effect of constant power loads in power converters and proposed the implementation of the Circular Switching Surfaces (CSS) for controlling the BCDU in electric vehicle systems in order to mitigate instability behavior.

CPL dynamics were investigated in a Buck+Boost cascade converter further implemented as the BCDU, interfacing with the energy storage and the HV DC link. Asynchronous and synchronous operating modes were investigated, identifying this last as the worst case operating condition, where oscillations grow without boundaries. As was shown with simulation as well as experimental results, the simple and practical geometric technique presented a solution for the challenging combination of high-bandwidth CPL and this unbounded oscillation due to synchronous operation of the converter, and yielded large-signal stability and enhanced dynamic transient response over a wide range of operating conditions required by the targeted application.

Comparison with state-of-the-art linear and non-linear controllers showed a transient recovery improvement of up to 3.4 times and a considerable reduction in switching actions, thereby improving efficiency. The control laws based on the CSS were derived from a normalized converter, generalizing the application. Furthermore, the analysis led to a theoretical framework in which predictable transient performance can be achieved.

The application of this control technique enables a reduction in the size of the bulky DC-link capacitance usually employed to stabilize the main bus. This allows the usage of

metal-film capacitors, which have reliability advantages over commonly employed electrolytic capacitors as well as reduced ESR, improving system efficiency. Reduction of the capacitance is very important as well since it allows for reductions in size, weight and finally the cost of the final implementation.

Experimental results were developed in a scaled $1kW$ Buck+Boost cascade converter to validate the concepts described and the application of the CCS for CPL transient rejection and steady-state operation.

The contributions of this thesis are supported by publication in IEEE APEC 2014 [1] and it is currently submitted under review with minor changes to IEEE Transactions on Power Electronics [2].

5.2 Future Work

BCDU are bidirectional power converters providing power flow to the traction system and recovering energy to the batteries through regenerative braking. The work developed in this thesis covered the motoring operation of the BCDU in which energy is delivered from the batteries to the traction systems and to the rest of the EV power system. To control the energy recovered from the electric motor to the battery set, a different control strategy is required that will shape the input current to the battery according to the SOC. The regenerative operation needs to be combined with dynamic braking due to the limitation in the amount of energy that can be stored in the batteries.

During this thesis work a high-power BCDU and motor drive platform were designed and constructed and requires integration to conform a high-power bidirectional motor drive platform for the development and testing of control techniques for energy management in EVs. This would allow to develop high performance control algorithms to achieve comprehensive regenerative braking as well as precision control of electric torque of the drive train.

Bibliography

[1] M. Anun, M. Ordonez, I. Galiano and G. Oggier, "Bidirectional Power Flow with Constant Power Load in Electric Vehicles: A Non-linear Strategy for Buck+Boost Cascade Converters," in *Proc. IEEE Appl. Power Electron. Conf. (APEC) 2014*, Fort Worth, TX, 2014.

[2] M. Anun, M. Ordonez, I. Galiano Zurbriggen, G. Oggier, "Circular Switching Surface Technique: High Performance Constant Power Load Stabilization for Electric Vehicle Systems," submitted under review with major changes to *IEEE Transactions on Power Electronics*, March 2014.

[3] T. Trigg and P. Telleen, "Global EV Outlook: Understanding the Electric Vehicle Landscape to 2020," IEA, Paris, France, 2013.

[4] D. Anair and A. Mahmassani, "State of CHARGE: Electric Vehicles Global Warming Emissions and Fuel-Cost Savings across the United States," UCS, Cambridge, MA, Rep. 02138-3780, 2012.

[5] H. Van Essen and B. Kampman, "Impacts of Electric Vehicles Summary report," CE Delft, Delft, Netherlands, Rep. 11.4058.26, 2011.

[6] A. Emadi, M. Ehsani, and J. M. Miller, "Automotive Power Systems," in *Vehicular Electric Power Systems: Land, Sea, Air, and Space Vehicles.*, New York: Marcel Dekker, Dec. 2003.

[7] Z. J. Shen, "Optimal Power Management and Distribution in Automotive Systems,"

in *Handbook of Automotive Power Electronics and Motor Drives*, A. Emadi Ed., Boca Raton, FL: CRC Press, 2005.

[8] O. Hegazy, R. Barrero, J. Van Mierlo, P. Lataire, N. Omar, T. Coosemans, "An Advanced Power Electronics Interface for Electric Vehicles Applications," *IEEE Trans. Power Electron.*, vol. 28, no. 12 pp. 5508-5521, Dec. 2013.

[9] N. A. Chaturvedi, R. Klein, J. Christensen, J. Ahmed, A. Kojic, "Algorithms for Advanced Battery-Management Systems," *IEEE Control. Syst. Mag.*, vol. 30, no. 3, pp. 49-68, June 2010.

[10] S. Waffler and J.W. Kolar, "A Novel Low-Loss Modulation Strategy for High-Power Bidirectional Buck+Boost Converters," Power Electronics, IEEE Transactions on , vol.24, no.6, pp. 1589-1599, June 2009.

[11] A. Khaligh, "Stability Criteria for the Energy Storage Bi-directional Dc/Dc Converter in the Toyota Hybrid System II," in *Proc. IEEE Veh. Power and Prop. Conf. (VPPC) 2007*, pp. 348-352, Sep. 2007.

[12] A. Emadi, S. S. Williamson, and A. Khaligh, "Power Electronics Intensive Solutions For Advanced Electric, Hybrid Electric, and Fuel Cell Vehicular Power Systems," *IEEE Trans. Power Electron.*, vol. 21, no. 3, pp. 567-577, May. 2006.

[13] R. M. Schupbach and J. C. Balda, "Comparing DC-DC Converters For Power Management in Hybrid Electric Vehicles," in *Proc. IEEE Elec. Mach. and Drives Conf. (IEMDC) 2003*, vol.3, pp. 1369-1374, June 2003.

[14] F. Caricchi, F. Crescimbini, F. Giulii Capponi, and L. Solero, "Study of Bi-Directional Buck-Boost Converter Topologies for Application in Electrical Vehicle Motor Drives," in *Proc. IEEE Appl. Power Electron. Conf. (APEC) 1998*, vol.1, pp. 287-293, Feb. 1998.

[15] F. Caricchi, F. Crescimbini, G. Noia, and D. Pirolo, "Experimental Study of a Bidirectional DC-DC Converter for the DC Link Voltage Control and Regenerative Braking in PM Motor Drives Devoted to Electrical Vehicles," in *Proc. IEEE Appl. Power Electron. Conf. (APEC) 1994*, vol.1, pp. 381-386, Feb. 1994.

[16] F. Caricchi, F. Crescimbini, A. Di Napoli, and M. Marcheggiani, "Prototype of Electric Vehicle Drive With Twin Water-Cooled Wheel Direct Drive Motors," in *Proc. IEEE Power Electron. Spec. Conf. (PESC) 1996*, pp. 1926-1932 , June 1996.

[17] Y. A-R I. Mohamed, A.A.A. Radwan, and T.K. Lee, "Decoupled Reference-Voltage-Based Active DC-Link Stabilization for PMSM Drives With Tight-Speed Regulation," *IEEE Trans. Ind. Electron.*, vol. 59, no. 12, pp. 4523-4536, Dec. 2012.

[18] X. Y. Liu, A. J. Forsyth, "Comparative Study of Stabilizing Controllers for Brushless DC Motor Drive Systems," in *Proc. IEEE Elect. Mach. and Drives Conf. (IEMDC) 2005*, pp. 1725-1731, May 2005.

[19] A. Emadi, A. Khaligh, C. H. Rivetta, and G. A. Williamson, "Constant Power Loads and Negative Impedance Instability in Automotive Systems: Definition, Modeling, Stability, and Control of Power Electronic Converters and Motor Drives," *IEEE Trans. Veh. Technol.*, vol. 55, no. 4, pp. 1112-1125, July 2006.

[20] A. M. Rahimi and A. Emadi, "An Analytical Investigation of DC/DC Power Electronic Converters With Constant Power Loads in Vehicular Power Systems," *IEEE Trans. Veh. Technol.*, vol. 58, no. 6, pp. 2689-2702, Jul. 2009.

[21] M. Cespedes, Lei Xing, and Jian Sun, "Constant-Power Load System Stabilization by Passive Damping," *IEEE Trans. Power Electron.*, vol. 26, no. 7, pp. 1832-1836, Jul. 2011.

[22] A. M. Rahimi and A. Emadi, "Active Damping in DC/DC Power Electronic Converters: A Novel Method to Overcome the Problems of Constant Power Loads," *IEEE Trans. Ind. Electron.*, vol. 56, no. 5, pp. 1428-1439, May 2009.

[23] A. M. Rahimi, G. A. Williamson, and A. Emadi, "Loop-Cancellation Technique: A Novel Nonlinear Feedback to Overcome the Destabilizing Effect of Constant-Power Loads," *IEEE Trans. Veh. Technol.*, vol. 59, no. 2, pp. 650-661, Feb. 2010.

[24] P. Magne, B. Nahid-Mobarakeh, S. Pierfederici, "General Active Global Stabilization of Multiloads DCPower Networks," *IEEE Trans. Power Electron.*, vol. 275, no. 4, pp. 1788-1798, Apr. 2012.

[25] C. N. Onwuchekwa and A. Kwasinski, "Analysis of Boundary Control for Buck Converters With Instantaneous Constant-Power Loads," *IEEE Trans. Power Electron.*, vol. 25, no. 8, pp. 2018-2032, Aug. 2010.

[26] C. N. Onwuchekwa and A. Kwasinski, "Analysis of Boundary Control for Boost and Buck-Boost Converters in Distributed Power Architectures with Constant-Power Loads," in *Proc. IEEE Appl. Power Electron. Conf. (APEC) 2011*, pp. 6-11, March 2011.

[27] Y. Zhao, W. Qiao, D.Ha, "A Sliding-Mode Duty-Ratio Controller for DC/DC Buck Converters with Constant Power Loads," *IEEE Trans. Ind. Appl.*, vol. 50, no. 2, pp. 1448-1458, Mar. 2014.

[28] R. Munzert, P. T. Krein, "Issues in Boundary Control [of Power Convertors]," in *Proc. IEEE Power Electron. Spec. Conf. (PESC) 1996*, pp. 810-916, June 1996.

[29] M. Ordonez, M. T. Iqbal, and J. E. Quaicoe, "Selection of a Curved Switching Surface for Buck Converters," *IEEE Trans. Power Electron.*, vol. 21, no. 4, pp. 1148-1153, Jul. 2006.

[30] K. K. S. Leung and H.S.-H Chung, "Derivation of a Second-Order Switching Surface in the Boundary Control of Buck Converters," *IEEE Power Electron. Lett.*, vol. 2, no. 2, pp. 63-67, Jun. 2004.

[31] T. Siew-Chong, Y. M. Lai, ; C. K. Tse, M. K. H.Cheung, "A Fixed-Frequency Pulsewidth Modulation Based Quasi-Sliding-Mode Controller for Buck Converters," *IEEE Trans. Power Electron.*, vol. 20, no. 6, pp. 1379-1392, Nov. 2005.

[32] J. M. Galvez, M. Ordonez, F. Luchino, and J. E. Quaicoe, "Improvements in Boundary Control of Boost Converters Using the Natural Switching Surface," *IEEE Trans. Power Electron.*, vol. 26, no. 11, pp. 3367-3376, Nov. 2011.

[33] M. Ordonez, J. E. Quaicoe, and M. T. Iqbal, "Advanced Boundary Control of Inverters Using the Natural Switching surface: normalized geometrical derivation," *IEEE Trans. Power Electron.*, vol. 23, no. 6, pp. 2915-2930, Nov. 2008.

[34] G.G. Oggier, M. Ordonez, J. M. Galvez, F. Luchino, "Fast Transient Boundary Control and Steady-State Operation of the Dual Active Bridge Converter Using the Natural Switching Surface," *IEEE Trans. Power Electron.*, vol.29, no.2, pp. 946-957, Feb. 2014.

[35] M. Salcone and J. Bond, "Selecting Film Bus Link Capacitors for High Performance Inverter Applications," in *Proc. IEEE Elect. Mach. and Drives Conf. (IEMDC) 2009*, pp. 1692-1699, May 2009.

[36] L. Gu, X. Ruan, M. Xu, and K. Yao, "Means of Eliminating Electrolytic Capacitor in AC/DC Power Supplies for LED Lightings," *IEEE Trans. Power Electron.*, vol. 24, no. 5, pp. 1399-1408, 2009.

[37] K. Yao, X. Ruan, X. Mao, and Z. Ye, "Reducing Storage Capacitor of a DCM Boost PFC Converter," *IEEE Trans. Power Electron.*, vol. 27, no. 1, pp. 151-160, Jan. 2012.

[38] T. Messo, J. Jokipii, J. Puukko, T. Suntio, "Determining the Value of DC-Link Capacitance to Ensure Stable Operation of a Three-Phase Photovoltaic Inverter," *IEEE Trans. Power Electron.*, vol.29, no.2, pp. 665-673, Feb. 2014.

[39] H. Wang, H. S. -H. Chung and W. Liu, "Use of a Series Voltage Compensator for Reduction of the DC-Link Capacitance in a Capacitor-Supported System," *IEEE Trans. Power Electron.*, vol. 29, no. 3, pp. 1163-1175, Mar. 2014.

[40] R. D. Middlebrook, "Input Filter Considerations in Design and Application of Switching Regulators," *in Proc. IEEE Ind. Appl. Soc. Annu. Meet.*, 1976, pp. 366382.

[41] P. C. Krause, O. Wasynczuk, and S. D. Sudhoff, "Induction Motor Drives," in *Automotive Power Systems.*, 2nd Ed. Piscataway, NJ: Wiley-Interscience , 2002.